Final Draft
of the original manuscript

Liang, C.; Xie, X.; He, Y.; Chen, H.; Yu, X.; Zhang, W.; Mi, H.; Lu, B.; Tian, D.; Zhang, H.; Li, M.; Zhou, Z.:

Multiple sediment sources and topographic changes controlled the depositional architecture of a palaeoslope-parallel canyon in the Qiongdongnan Basin, South China Sea.

In: Marine and Petroleum Geology. Vol. 113 (2020) 104161.

First published online by Elsevier: 06.12.2019

https://dx.doi.org/10.1016/j.marpetgeo.2019.104161

Multiple sediment sources and topographic changes controlled the depositional architecture of a palaeoslope-parallel canyon in the Qiongdongnan Basin, South China Sea

Chao Liang[a], Xinong Xie[a,*], Yunlong He[a,], Hui Chen[a], Xiaohang Yu[a], Wenyan, Zhang[b], Honggang Mi[c], Biyu Lu[a], Dongmei Tian[a], Hui Zhang[c], Mingjun Li[c], Zhan Zhou[c]**

[a] *College of Marine Sciences and Technology, China University of Geosciences, Wuhan 430074, China*

b Institute of Coastal Research Helmholtz Center, Geesthacht 21502, Germany

c Zhanjiang Branch of China National Offshore Oil Corporation, Zhanjiang 524057, China

Abstract

Submarine canyon deposits have drawn attention due to their significance on source-to-sink analysis and hydrocarbon exploration. High-resolution 2-D and 3-D seismic and exploration well data recently collected in the Ledong-Lingshui segment of the Qiongdongnan Basin are used to investigate the depositional architecture of the palaeoslope-parallel Central Canyon, which is distinct from other slope-perpendicular canyons. This study indicates that the canyon developed along the thalweg of a multiple stepped palaeotopography with a slope-parallel descending trend eastwards. The location of the thalweg is controlled by regional tectonics and progradational slope clinoforms in the western Qiongdongnan basin. Geographic changes in an extending direction and slope gradient of the palaeotopography resulted in variations in the depth and width of the canyon. Analysis of the canyon infillings indicates multiple sediment sources including an axial sediment source from the Central Vietnam and the western Hainan Island and a canyon-side source from the northern slope of the Qiongdongnan basin. Provenance study shows that the former source supplied relatively coarse-grained turbidites and the later supplied fine-grained mass transport deposits (MTD). Most of such MTDs originated from the northern slope of the basin. Evolution of the Central Canyon can be classified into three stages. Stage 1 is characterized by significant incisions that are responsible for the formation of the canyon. Subsequently or contemporaneously, the sharp bend at the beginning of the middle segment of the canyon likely resulted in lateral erosion, which triggered large-scale and small-scale canyon margin failures in the middle and lower segments of the canyon, respectively. The subsequent early filling stage (Stage 2) refers to the deposition of turbidites supplied by the axial sediment source. However, the morphology of the stepped thalweg slope resulted in sediment bypass in the upper segment of the Central Canyon. During the late filling stage (Stage 3), MTDs supplied by the canyon-side sediment source were dominated, and interbedded with turbidite deposits. The deposition of the MTDs resulted in the sharp decreases in canyon accommodation space and the abrupt southeastwards stepping of the deepest part of the canyon. Moreover, complex interactions between debris-flows and turbidity-flows occurred during this stage. Such variations in architecture of the canyon were controlled by multiple sediment supplies and topographic changes. The proposed conceptual model of canyon infilling and the resulting stratigraphic architecture could be applied in other analogous canyons for hydrocarbon exploration.

Keywords: Deep-water canyon; Stratigraphic architecture; Stepped-thalweg slope; Multiple sediment supplies; Decompaction

1. Introduction

Submarine canyons, the primary conduits for transporting sediments from the continental shelf to the deepwater area (Babonneau et al., 2002; Popescua et al., 2004; Antobreeh and Krastel, 2006; Lo Iacono et al., 2014), have drawn the attention of numerous studies because they offer abundant information of tectonic and stratigraphic evolution, and climatic and sea-level changes of continental margins (e.g. Wonham et al., 2000; Gingele et al., 2004; Antobreeh and Krastel, 2006; Yoshikawa and Nemoto, 2010; Umar et al., 2011; Talling, 2015; Flecker et al., 2015 and Vesely, 2015) as well as significant hydrocarbon reservoir discoveries within the canyon fillings (e.g. Crossey et al., 2006; Mayall et al., 2006; Fuh et al., 2009). Generally, the evolution of a submarine canyon is characterized by erosion in the early stage, which is triggered by relative sea-level fall that results in an erosional container filled with sediments in the later stage owing to subsequent relative sea-level rise (e.g. Babonneau et al., 2002; Deptuck et al., 2003 and 2007; Catterall et al., 2010). The majority of the reported submarine canyons are in general perpendicular or oblique to the continental slopes because canyon development is controlled mainly by downslope gravity processes (e.g. Gingele et al., 2004; Crossery et al., 2006; Harris et al., 2011; Iacono et al., 2014; Bouroullec et al., 2017). However, in certain circumstances canyons may run parallel or sub-parallel to continental slopes owing to particular structural settings. For example, the Central Canyon exhibits a slope-parallel development controlled by the elongate slope-parallel No. 2 Fault and other basement faults in the Qiongdongnan Basin (Fig. 1A) (Gong et al., 2011). The architectures of slope-perpendicular canyons have been widely documented and discussed regarding both passive and active continental margins during the last decades (e.g. Shepard and Emery, 1973; Nagel et al., 1986; Pratson et al., 1994; Deptuck et al., 2003 and 2007; Bertoni et al., 2005; Di Celma et al., 2014; Gamberi et al., 2015; Mauffrey et al., 2017). Their architectures are generally related to a single sediment source, physiographic changes, tectonic evolution, sea-level changes, or climatic changes such as sea-level variation. However, the palaeoslope-parallel Central Canyon in the Qiongdongnan Basin was supplied by both axial and side sediment sources, resulting in distinct architectures compared with other slope-perpendicular canyons (e.g. Gong et al., 2011).

In the past few years, the depositional architectures of the Central Canyon in the eastern segments of the Qiongdongnan Basin have been analysed and discussed (e.g. Gong et al., 2011; Su et al., 2014; Wu et al., 2018). The accurate time at which the sediments supplied by the side sediment source began to be dumped into the canyon differs among these studies. The sedimentary infilling processes within the canyon show a gradually decreasing input from the axial sediment source and an increasing supplement from the side sediment source upwards (Gong et al., 2011; Wu et al., 2018). In general, the sediments supplied by the axial sediment source are composed of coarse-grained turbidites, whereas those supplied by the side sediment source are dominated by fined-grained mass transport deposits (MTDs) (e.g. Gong et al., 2011; Wu et al., 2018). These features help us to understand the vertical evolution of the canyon in our study area, that is, the Ledong–Lingshui segment of the canyon (Fig. 1). However, changes in the depositional architecture along the canyon pathway caused by topographic changes have so far not been considered in previous studies. Our observations indicate that these changes are characterised by a stepped-thalweg slope along the canyon pathway, and the canyon fillings show a complex interplay between the axial sediment supply, the side sediment supply, and the topographic changes. Additionally, recent hydrocarbon exploration wells provide critical information to further our understanding of the depositional architecture of the canyon.

Based on analysis of high-resolution two-dimensional (2D) and three-dimensional (3D) seismic data, well logs, and lithologic data, the objectives of this study are: (i) to quantify the geomorphology of the canyon, specifically width, depth, and thalweg slope gradient, in the Ledong–Lingshui segment of the Qiongdongnan Basin; (ii) to describe and interpret the seismic facies and reveal the internal architecture patterns; and (iii) to discuss the effects of multiple sediment supplies and topographic changes on the depositional architecture of the palaeoslope-parallel canyon.

2. Geological setting

The Qiongdongnan Basin, one of the Cenozoic petroliferous basin located in the northwestern margin of the South China Sea (Xie et al., 2008; Yu et al., 2009; Su et al., 2012; Wang et al., 2015; Huang et al., 2015), has an area of about 45, 000 km^2 (Fig. 1A) (Su et al., 2014). The basin is bounded by the Red River Fault to the west, the Hainan Islands to the north, the Pearl River Mouth Basin to the northeast, and the Xisha Uplift to the south (Fig. 1) (Zhu et al., 2009; Li et al., 2013; Su et al., 2014; Ma et al., 2017; Li et al., 2017a). Tectonic evolution of the Qiongdongnan Basin has experienced two stages: (i) a rifting stage (Eocene to Oligocene), marked by the multiple episodes of rifting, which formed a series of subbasins that are downthrown to the south; (ii) a post-rift stage (Miocene to Holocene), including the thermal subsidence and accelerated subsidence sub-stages separated by the regional discontinuity T40 (11.6 Ma) (Fig. 2) (Gong and Li, 1997; Xie et al., 2008; Wu et al., 2008; Zhu et al., 2009; Hu et al., 2013; Morley, 2016). Basin filling in the Qiongdongnan Basin consists of the lower rift supersequence and the upper post-rift supersequence separated by the regional discontinuity T60 (23 Ma) (Gong et al., 2011). The former contains the marsh to coastal plain Yacheng Formation and littoral Lingshui Formation, and the latter is composed of the littoral to neritic Sanya and Meishan Formations, as well as the bathyal to abyssal Huangliu, Yinggehai and Ledong Formations (Fig. 2).

The Central Canyon in the Qiongdongnan Basin has a length of more than 425 km, and a width ranging from 3km to 16 km (Gong et al., 2011). The canyon shows an overall W-E extending S-shaped geometry in plan-view (Su et al., 2014) (Fig. 1), which is suggested to occur during the accelerated subsidence sub-stage (Fig. 2) (Su et al., 2009). The Ledong-Lingshui segment of the Central Canyon is the focal point of this study (Fig. 1). The canyon in the western study area had incised into the strata of T31-T30 (8.2-5.7 Ma), but did not penetrate the discontinuity T31 (8.2 Ma) (Fig. 3C). Moreover, the canyon was fully filled at the discontinuity T29 (4.2 Ma) (Figs. 3). Thus, the canyon infill stage in the study area is inferred to commence after 8.2 Ma, and terminate at 4.2 Ma.

3. **Data and Methods**

The data used in this study were provided by the China National Offshore Oil Corporation (CNOOC), including an industry acquired 3D seismic volume with an area of 2000 km^2, several high-resolution 2D seismic profiles with a total length of 200 km, well log and lithologic data collected from two exploration wells, and a 3D velocity model of the strata in the Qiongdongnan Basin. The dominant frequency of these seismic data is approximately 30 Hz, with a vertical resolution of ~25 m and the sample rate of 4 ms. Bin spacing of the 3D seismic data is 25 m × 12.5 m and the 2D seismic data have a trace spacing of 12.5 m. These seismic data were processed to zero phase and presented using “SEG reverse polarity”.

Synthetic seismic records were generated using the sonic, density logs, well tops, time-depth relationship data, and the 3D seismic data (Fig. 4). Then the records were used for seismic-well tie to determine the key seismic reflections (T40, T31, T30, T29, T27 and T20), and the tops and bases of the depositional units (DU2-6) within the canyon (Fig. 4). The tops and bases of DU1 and DU7 were discerned through the observation of amplitudes, continuities, truncations, onlaps and downlaps of the seismic data. All these discontinuities were traced in the whole study area. The seismic data were interpreted using Geoframe 2012. The seismic attribute toolkit module in Geoframe 2012 was utilized to get RMS attribute and coherence slice maps. Additionally, 2D visualization module in Petrel 2011 was used to generate the topographic map of the canyon in Fig. 3A.

Numerous line measurements were taken to determine the morphological parameters of the canyon such as thalweg slope gradient, width, and depth (Fig. 3A). The canyon was subdivided into three parts: canyon thalweg, canyon wall, and canyon flank (Figs. 3A and 3B). The canyon thalweg is the deepest part of the canyon, and the adjacent steep margins are referred to as canyon walls; the canyon flanks represent the relatively gentle sections on either side of the canyon walls (Figs. 3A and 3B). Like the quantitative methods used by Catterall et al. (2010), the width of the canyon is defined as the horizontal distance between the inflection points in the cross-section, and the depth is defined as the average value of the vertical differences between the thalweg and the inflection points in the cross-section (Fig. 3B).

Horizon data of key seismic reflections in the thalweg longitudinal profile such as basal erosion surface, T30, T27, T20, and the modern seafloor (Fig. 3C) were imported into Petrel 2011 software and were converted from time to depth using the 3D velocity model, which was established by China National Offshore Oil Corporation (CNOOC) based on the velocity spectrum data collected from numerous wells in the Qiongdongnan Basin. Then, the horizon data were imported into 2D Move™ software, and a 2D decompaction workflow was conducted to obtain the original geomorphology of the thalweg slope of the canyon. The stripped-off strata were shown in Fig. 3C. During the process of decompaction, standard values of 0.51 and 0.51 were used for coefficients of porosity and depth, respectively (e.g. Catterall et al., 2010). Differences in the tectonic subsidence within the study area were not obvious (e.g. Li et al., 2013), and thus tectonic subsidence was not considered after the decompaction workflow.

4. Results

4.1 Geomorphology of the canyon

Based on geomorphological changes of the canyon including trend, thalweg slope gradient, width, and depth, the canyon was subdivided into three segments within the Ledong–Lingshui Depression: (i) Upper Reach; (ii) Middle Reach, and (iii) Lower Reach. In general, the canyon is characterised by an overall V-shaped plan-form geometry as seen in plan view (Figs. 3A) and a stepped-thalweg slope along its pathway (Figs. 3C and 5A,). Moreover, three knickpoints (K1-K3) were observed in the thalweg slope profile (Fig. 5A). To quantify the geomorphology of the canyon, the canyon thalweg in the first measuring line (i.e. in the northwestern-most corner of the study area (Fig. 3A) is referred to as the origin of the x-axis in Fig. 5. The Upper Reach is present over the first 21.5 km, and the Middle Reach is located between 21.5 and 54.3 km (Fig. 5A). The Lower Reach is the shortest segment of the canyon in the study area, extending from 54.3 to 60.1 km (Fig. 5A).

In the Upper Reach, the canyon is slightly sinuous (with the sinuosity of 1.01°) and has a WNW to ESE trend (Fig. 3A). The boundary between the canyon wall and canyon flank is not very clear because the widths of the canyon flanks of both sides are fairly narrow (Fig. 3A). The Upper Reach is characterised by a gentle thalweg slope. Over the first 13.7 km, the thalweg slope is about 0.17°. However, between 13.7 and 21.5 km, a convex-up section of the thalweg longitudinal profile, at about 0.5–2°, was observed (Fig. 5A). The depth of the canyon has a range of 288.0-445.5 m (Fig. 5A and Table 1). At 21.5 km, the minimum depth of the canyon corresponds to the maximum point of the thalweg convexity (Fig. 5A). Additionally, a constant increase in the width of the canyon (from 4.1 km to 9.2 km wide) was observed throughout the Upper Reach. In the first 11.4 km, the width of the canyon increases slowly (from 4.1 km to 5.5 km wide), and increases rapidly between 5.5 and 21.5 km, reaching a width of 8.9 km at the boundary with the Middle Reach (Fig. 5B). Knickpoint K1 at 21.5 km marks the boundary between the Upper and Middle Reaches (Fig. 5A), after which point the thalweg slope becomes steeper, and the increase of the canyon width ends abruptly (Fig. 5).

In the Middle Reach, the canyon is characterised by a slight S-shaped geometry as seen in plan view (with the sinuosity of 1.14) and has an overall SW–NE orientation (Fig. 3A). Downslope between 21.5 and 30.9 km, the canyon trends ESE and then changes sharply to NE at 30.9 km (Fig. 3A). A concave-up thalweg longitudinal profile is present throughout the Middle Reach, which exhibits more sinuous plan-form morphology (with the sinuosity of 1.14°) than that in the Upper Reach (1.01°) and the Lower Reach (1.00°), as shown by the red solid line in Fig. 3A. Within the initial part of the Middle Reach (21.5–25.5 km), the thalweg slope is relatively gentle, at about 0-2°; however, the adjacent part in the downstream direction (25.5-30.9 km) is the steepest part of the entire study area, at about 3-6° (Fig. 5A). Note that the convex-up section between 21.5 km and 30.9 km (circled in Fig. 5A) probably resulted from the velocity model because this abnormal phenomenon was not observed in time domain (see the basal erosion surface in Fig. 3C). Between 30.9 and 34.0 km, a gentle thalweg slope of about 0.5° was observed. Knickpoint K2 marks the boundary between this gentle section and the following relatively steep section (1–3.5°) in the downstream direction (34.0–35.9 km) (Fig. 5A). The remaining part of the Middle Reach (35.9-54.3 km) is characterised by a gentle thalweg slope of about 0.5–1.5° (Fig. 5A). The depth of the canyon increases rapidly between 21.5 and 30.9 km, reaching at depth of 720.5 m at 30.9 km. The depth of the canyon shows little change (720.5-797.2 m deep) throughout the remaining part of the Middle Reach (30.9-54.3 km) (Fig. 5A). It is noteworthy that between 44.1 and 54.3 km, the width of the canyon (10.8–16.7 km wide) is significantly larger than that in the adjacent parts (Fig. 5B). Throughout the initial part of the Middle Reach between 21.5 and 34.6 km, an overall increase in canyon width (from 8.9 km to 13.0 km wide) was observed (Fig. 5B). However, a little change (12.9-13.9 km wide) was observed between 34.6 and 44.1 km (Fig. 5B).

Knickpoint K3 marks the boundary between the Middle and Lower Reaches (Fig. 5A). The canyon has an approximately WSW–ENE orientation in the Lower Reach (Fig. 3A) and is characterised by a gently concave-up thalweg slope profile of about 0-3° (Fig. 5A). The width of the canyon declines abruptly to 9.3 km at knickpoint K3 (Fig. 5B). An overall increase in canyon depth (from 751.5m to 1032.2 m deep) is present throughout the Lower Reach.

4.2 Seismic facies and depositional interpretations

On the basis of observed seismic reflection changes, such as those in amplitude, continuity, frequency, and external geometry, seven seismic facies were discerned and calibrated with the well logs and lithological data collected from two exploration wells (wells A and B in Figs. 1B and 3A).

Seismic facies 1 (Fig. 6A) appears in the vertical seismic profile as high-amplitude, low-frequency, high-continuity and sub-parallel reflections that onlap against the canyon walls. The lithological data and gamma ray (GR) log from well A (Fig. 6B) indicate three fining-upward successions each composed of lower thick-bedded sandstone and upper thin-bedded silty mudstone/mudstone. The sandstones were characterised by massive beddings and were interpreted as the Ta divisions of the Bouma sequence (Li et al., 2017a). The thin-bedded silty mudstones/mudstones are interpreted as the Te divisions of the Bouma sequence, representing the final period of fine-grained suspension sedimentation of turbidity currents (e.g. Lowe, 1982). The lithofacies associations were interpreted as high-density turbidity current deposits, which have been well documented in previous studies (e.g. Lowe et al., 1982; Baas et al., 2004; Olariu et al., 2011; Li et al., 2017).

Seismic facies 2 (Fig. 6C) consists of moderate frequency, low–moderate amplitude, and moderate–high continuous reflections. The lithological data and GR log from well A (Fig. 6D) reveal multiple fining-upward successions. Each succession is commonly characterised by thin-bedded sandstone, siltstone, or muddy siltstone in the lower part and thin-bedded silty mudstone or mudstone in the upper part. The sandstone and siltstone are interpreted as the Tb and Tc divisions of the Bouma sequence, respectively, formed by traction sedimentation of lower-density turbidity currents (e.g. Lowe, 1982; Campion et al., 2003; Joubert et al., 2010; Li et al., 2016). The muddy sandstone is interpreted as mixed traction and suspension sedimentation of lower-density turbidity currents, or the Td division of the Bouma sequence (e.g. Lowe et al., 1982). The silty mudstone and mudstone are interpreted as suspension sedimentation of lower-density turbidity currents in the final period (the Td division of the Bouma sequence) (e.g. Lowe et al., 1982), as documented by Li et al. (2016) in the typical turbidite outcrop at San Clemente. The silty mudstone at the uppermost part of the lithological column in Fig. 5D has a total thickness of 60 m. It was likely formed by multiple low-density turbidity flow events, in which main bodies of the turbidity flows bypassed downslope, and only the tails of the flows were deposited at that location (e.g. Brooks et al., 2018).

Seismic facies 3 (Fig. 6E) is characterised by high-amplitude reflection patches laid upon the basal erosion surface and consists of one or two seismic events. Wu et al. (2018) reported the same seismic facies in the eastern Lingshui segment of the Central Canyon, and interpreted the seismic facies as basal lag deposits that are generally composed of sand or mud-clast conglomerates (Mayall et al., 2006). Janocko et al. (2013) reported the similar seismic facies and deposits in the submarine sinuous channel belts offshore West Africa.

Seismic facies 4 (Fig. 6F) shows high-frequency, moderate-amplitude, high-continuity, and parallel seismic reflections. It is interpreted as hemipelagic deposits (Gong et al., 2011; Su et al., 2014; Li et al., 2017a).

Seismic facies 5 (Fig. 6G) consists of low-amplitude and chaotic reflections with sheet-like geometries. The lithological data from well B indicates that these seismic facies is characterised mainly by muddy deposits; sand deposition is very limited. They are interpreted as debris flow deposits, such as those documented by Gamberi et al. (2011) in the Gioia Basin of the southeastern Tyrrhenian Sea, Gong et al. (2014) in the Qiongdongnan Basin, and Sun et al. (2017 and 2018) in the Pearl River Mouth Basin of the South China Sea.

Seismic facies 6 (Fig. 6H) exhibits slightly disturbed, low-amplitude, low-moderate continuity reflections, with the seismic package characterised by slightly clockwise rotation. It can be interpreted as slide block formed by the collapse of the canyon margin. In the studies of Deptuck et al. (2007) and Janocko et al. (2013), the same seismic facies were found within the Benin-major Canyon in the western Niger Delta slope and in the sinuous channel belts offshore West Africa, respectively.

Seismic facies 7 (Fig. 6I) is commonly made up of low-amplitude, semi-transparent to chaotic seismic reflections with irregular cross-sectional and plan-form morphologies occurring locally in the Lower Reach. This is interpreted as slump deposits formed by gravitational instability in the canyon margin, as reported by Gong et al. (2014), Su et al. (2014). In summary, seismic facies 5, 6, and 7 all correspond to sediments driven directly by gravity rather than interstitial fluid motion (Middleton and Hampton, 1976), which are defined as mass-transport deposits (MTD) (Nardin et al., 1979). Two or more MTDs can be termed as mass-transport complex (MTC) (e.g. Canals et al., 2004; Shipp et al., 2011; Olafiranye et al., 2013; Gong et al., 2014).

4.3 Depositional units and facies association within the canyon filling

Based on observation of seismic reflection configuration (frequency, continuity and amplitude) and striatal terminations (onlap, downlap and truncation), seven depositional units (DU1 through DU7, upwards) were recognized within the canyon filling (Fig. 7) .

DU1 is characterized by three slide blocks presented in the Middle Reach (Fig. 8), and slump deposits and basal lags in the Lower Reach (Fig. 7F). These slide blocks are characterized by grey coherence patterns with crescent-shaped plan-form morphology (Fig. 8A) and show low-amplitude, low–moderate continuity, and slightly disturbed reflections in the vertical seismic profiles (Figs 7A, 7D, 8B, and 8C). Slide blocks 1, 2, and 3 (Fig. 8A) are all located in the outer bank sides of the canyon. Slide block 1, situated in the proximal part of the Middle Reach, has an area of 27.9 km^2 and a maximum thickness of 671.0 m (Fig. 9A). The long axis of slide block 1 displays a WNW–ESE orientation (Fig. 8A), whereas the long axis of slide blocks 2 and 3 trend NE (Fig. 8A). Slide block 3, present in the distal part of the Middle Reach, is larger than the other two slide blocks and covers an area of 46.78 km^2, with a maximum thickness of 529.3 m (Fig. 9A). Slide block 2, the smallest one, is characterised by an area of 11.06 km^2 and a maximum thickness of 311.3 m (Fig. 9A). It is worth noting that these slide blocks were severely eroded by subsequent turbidity currents in the centre of the canyon (Figs. 7D, 8B, and 8C). The thicknesses of the slump deposits and basal lags in the Lower reach range from 0 m to 266.5m, averaging 128.7 m (Fig. 9A and Table 1).

DU2 is characterised by thick-bedded high-density turbidity current deposits in the Middle and Lower Reaches and thin-bedded low-density turbidity current deposits in the Upper Reach (Figs. 7, 8B and 8C). The thin-bedded low-density turbidity current deposits are marked by relatively consistent thicknesses (Fig. 9B) averaging 44.6 m (Table1), whereas the thick-bedded high-density turbidity current deposits exhibit variable thicknesses ranging from 0 to 435.1 m with an average thickness of 137.2 m (Fig. 9B and Table 1).

DU3 is marked by low-density turbidity current deposits covering the entire canyon in the study area (Fig. 7). Significantly, the thickness of the low-density turbidity current deposits in the Upper Reach, averaging 50.4 m, is still less than that of the Middle and Lower Reaches, which have an overall consistent thickness averaging 86.1 m (Fig. 9C and Table 1).

DU4 consists of high-density turbidity current deposits located in the Upper Reach and in the southwestern part of the Middle Reach. An MTD is present in the Lower Reach and in the northeastern part of the Middle Reach (Figs. 7 and 10). The high-density turbidity current deposits show high root–mean–square (RMS) values in the RMS map (Fig. 10B) with an area of approximately 230 km^2, corresponding to sand-rich deposits. The thickness of the high-density turbidity current deposits shows a slight increasing trend along the canyon pathway (Fig. 9D), averaging 60.9 m in the upper reach and 85.3 m in the southwestern part of the Middle Reach (Table 1). On the contrary, the MTD is dominated by low RMS values because the MTD is composed mainly of muddy deposits, and it covers an area of about 250 km^2. The flattened coherence slice map (Fig. 10A) shows characteristics similar to those presented in the RMS map. The MTD displays a dark-coloured coherence pattern, whereas the high-density turbidity current deposits exhibit a light-coloured coherence pattern (Fig. 10A). The uniform thickness of the MTD along the canyon pathway is observed (Fig. 9D), with an average value of 154.3 m.

DU5 is composed of high-density turbidity current deposits only (Figs. 7 and 11). The high-density turbidity current deposits are dominated by high RMS values in the RMS map (Fig. 11A). It is important to note that in the northeastern part of the Middle Reach, where MTD occurs in the underlying DU4, the high-density turbidity current deposits could not cover the entire canyon; several areas marked by low RMS values are observed (Fig. 11). The thickness of DU5 is relatively uniform along the canyon pathway (Fig. 9E), with the average values of 62.4 m in the Upper Reach, 57.0 m in the Middle Reach, 63.6 m in the Lower Reach (Table 1). Note that the anomalies in Fig. 9E resulting from the adopted velocity model, was not observed in time domain. The Upper Reach of the canyon was filled completely during the DU5 deposition (Fig. 7C).

DU6 is composed of MTC1 through MTC4 in the Middle and Lower Reaches (Fig. 12A). These MTCs within the canyon show dark-coloured coherence patterns with convex-downslope plan-form geometries as seen in plan view (Fig. 12A). Moreover, pressure ridges in MTCs 2 and 3 are convex to the southeast in plan view (Fig. 12 A). MTC1 through MTC4 have, within the canyon, areas of approximately 73, 242, 268, and 200 km^2, respectively. In general, these MTCs thin gradually from the northwestern canyon flank averaging 450 m pinching-out towards the southeastern canyon flank in the Middle and Lower Reaches (Figs. 9F and 12B). Therefore, these MTCs display overall wedge-like geometries in the vertical seismic profiles (Figs. 7D, 7E, 7F and 12B). The main body of MTC1 lies in the Upper Reach (Fig. 12A), in which the canyon has already been filled completely during the DU5 deposition.

DU7 is only composed of low-density turbidity current deposits, which cannot be exhibited completely due to the limited data. Its thickness shows an increasing trend along the canyon pathway (Fig. 9G), and it has the average thickness of 29.9 m in the upper reach, 89.0 m in the middle reach and 98.0 m in the lower reach (Table 1). In the lower part of DU7, a sinuous channel about 0.48–1.52 km wide and averaging 29.9 m deep (Table 1) occured. The channel is characterized by an overall V-shaped plan-form geometry as seen in plan view (Fig. 12A), with a sinuosity of 1.25, which can be traced in the entire study area (Fig. 12). However, in the upper part of DU7, the channel disappears in the Middle and Lower Reaches and resumes in the Upper Reach (Figs. 12B, 12C, and 12D), where the canyon was filled completely during the DU5 deposition.

5. Discussions

5.1 Origin of the Central Canyon

Since the Early Miocene, the Qiongdongnan Basin evolved into the post-rift subsiding stage, and marked tectonic subsidence occurred in the Central Depression Belts (Fig.1B) (Shang et al., 2015). Thus, the longitudinal confined sag between the Central Uplift and the Southern Uplift began to develop (e.g. Shang et al., 2015). As the basin evolved into the Late Miocene, the continental slope system began to prevail in the northern margin of the Central Depression Belts (Xie et al., 2008). Therefore, the elongated negative-relief confined between the northern continental slope and the Southern uplift occurred in the Central Depression Belts. Moreover, the negative-relief was shallower in the west and deeper in the east, trending NE (Shang et al., 2015), probably with a bell-mouth shape. Subsequently, with the formation of the Ledong Fan in the Ledong Depression (Figs. 3C and 13) (see the detail descriptions in Wang et al., 2011; Li et al., 2017b; Li et al., 2019), the deepest part of the negative-relief in the Ledong Depression stepped gradually into the northern margin of the Ledong Depression. This negative relief was likely confined between the northern continental slope and Ledong Fan (Fig. 13) with an ESE trend and minor depths. However, in the Lingshui Depression, the negative-relief was still deep and confined between the northern continental slope and the Southern Uplift (Fig. 12B), with a NE trend. This likely resulted in development of the original negative relief with V-shaped plan-form geometry and a stepped thalweg slope. The Initiation of the Central Canyon has been well attributed to the significant incisions caused by large-scale and high-energy turbidity currents, which were supplied by the axial sediment source since 11.6 Ma when relative sea level in the Qiongdongnan Basin dropped (Fig. 2) (e.g. Li et al., 2011; Zhang et al., 2013). Therefore, the original negative relief accumulated the turbidity currents and served as a fairway to promote the formation of the Central Canyon.

The Upper Reach of the canyon (averaging 378.6 m deep) is obviously shallower than the Middle Reach (averaging 649.1 m deep) and the Lower Reach (averaging 919.6 m deep) (Fig. 5A and Table 1), which can be attributed to limited incisions. As the stepped palaeotopography at that location was gentle, turbidity currents had the lowest velocity and erosional ability. The canyon depth in the Middle Reach was apparently greater than that in the Upper Reach (Fig. 5A). That is, erosive turbidity currents had relatively higher flow velocities and erosional capacities within the segment owing to the existence of the steeper ramp at the beginning of the Middle Reach (Fig. 5A). Although the stepped palaeotopography was relatively gentle in the Lower Reach, the accelerated turbidity currents likely could not decelerate within a short distance, which could have increased the flow velocity, leading to the deepest canyon (Fig. 5A). Because depth of the canyon was gradually increasing, the sharp change in the trend of the canyon at the start of the Middle Reach, from ESE to NE, likely forced the turbidity currents toward the canyon walls, giving rise to lateral erosion. Moreover, this effect might have gradually decreased to zero with distance from the sharp bend. This theory can be applied to interpret the widest Middle Reach (averaging 12.5 km wide) and the wide Lower Reach (averaging 10.3 km wide) (Table 1). It is noteworthy that width of the canyon decreases abruptly at the junction between the Middle and Lower Reaches (Fig. 5B). This is attributed to the presence of slide block 3 at that location (Fig. 8A), which was formed by destabilisation of the canyon margin resulting from the lateral erosion. Similar occurrences have been documented by Deptuck et al. (2007) in the Pleistocene Benin-Major Canyon (Niger Delta Slope) and by Janocko et al. (2013) in the submarine channel belts offshore West Africa.

5.2 Provenance of the canyon filling

Very recently, detrital zircon U–Pb chronological analysis and the rare earth element (REE) geochemical results of numerous samples collected from the upper Miocene sediments within the exploration wells (see their well locations in Fig. 1B) have revealed that the sedimentary infilling process within the western Central

Canyon were provinient from Central Vietnam, but the western Hainan Island is also an important sediment source (Cui et al., 2018). These supplied the axial sediment source. Equally, no channel, gully, or other erosion surface was observed on both sides of the canyon in the study area, indicating that the canyon filling during the Late Miocene (DU1 through DU3, upwards) was supplied dominately by the axial sediment source. Additionally, the detrital zircon U–Pb ages of three greyish-green fine-grained sandstone samples collected from well B (Fig. 1B) within a depth range of about 4686–4692 m (belonging to the different beds in DU2) show two dominated Indosinian (220–270 Ma) and Caledonian (420–440 Ma) populations (see Fig. 3B in Chen et al., 2015). These ages are similar to the age signatures of Central Vietnam, providing the similar evidences.

The MTD within DU4 (Fig. 7B and 10) is inferred to be sourced from the northwestern continental slope (side sediment supply) owing to the convex-downslope plan-form geometry as seen in plan view (Fig. 10A) and the headscarp dipping towards southeast (Fig. 12B). However, the high-density turbidity current deposits within DU4, DU5, and DU7 (Figs. 7B, 10, 11, and 12) were likely supplied by the axial sediment source, as evidenced by the absences of channels, gullies, or erosion surfaces on the contemporaneous sides of the canyon. Within DU6, the canyon filling is composed of four MTCs (MTC1 through MTC4 in Fig. 12A). MTC2 through MTC4 both show convex-downslope plan-form geometries as seen in plan view (Fig. 12A), and the headscarp also dips southeastwards (Fig. 12B). Moreover, the pressure ridges observed at the toe domains of MTCs 2 and 3 are convex to southeast as seen in plan view (Fig. 12B). These evidences indicate that MTCs2, 3 and 4 have the same flow direction from NW to SE, which is the dip of the continental slope in the Middle and Lower Reaches, like those reported by Frey-Martinez et al. (2005), Bull et al. (2009), Gong et al. (2014), and Gamboa and Alves et al. (2016). It is rather remarkable that MTC1 also flowed from NW to SE but turned to flow along the canyon path; this movement was likely influenced by the slope-parallel negative topography. The low-density turbidity current deposits within DU7 were supplied by the axial sediment source because the supplied channel can be traced into the Upper Reach, where a topographic high exists (Figs. 12A and 12C). Generally, DU4 through DU7 within the canyon were dominated by MTDs sourced from the northern continental slope (Fig. 7B), in which the shelf-edge deltas were supplied by the Lingshui and Wanquan rivers in southern and southeastern Hainan Island (Cao et al., 2015). The detrital zircon U–Pb chronological analysis and REE geochemical results of numerous samples collected from the Pliocene sediments within the exploration wells (see their well locations in Fig. 1B) show a increased input from Hainan Island and a decreasing trend in Central Vietnam during the Pliocene (Cui et al., 2018). This is in agreement with our observations.

5.3 Evolution stages of the Central Canyon

Based on the observations and analyses presented above, the evolution process of the canyon in the Ledong-Lingshui segment of the Qiongdongnan Basin (South China Sea) was reconstructed for the first time. The canyon evolved through three phases: (1) the incising stage; (2) the early filling stage, when sediments were supplied by the axial sediment source; and (3) the late filling stage, during time which sediments were supplied by both axial and side sediment sources.

5.3.1 Incising stage

During the incising stage, large volumes of erosive turbidity currents supplied by the axial sediment source during a sea-level fall incised the original negative-relief to form the canyon. These erosive turbidity currents bypassed and transported their main sediment loadings onto canyon mouth fans in the northwestern sub-basin of the South China Sea (e.g. Li et al., 2017b). Subsequently or contemporaneously, basal lags (DU1) were deposited in the study area (Figs. 7B, 7F, and 14A). Moreover, the sharp bend at the beginning of the Middle Reach, where the trend of the canyon changes from ESE to NE, likely resulted in lateral erosion, which triggered the collapse of the canyon walls. The lateral erosion effects decreased with distance from the sharp bend. This explains the large-scale canyon margin failures (DU1) that developed in the Middle Reach (Figs 7D, 8, and 14A), whereas small-scale canyon margin failures (DU1) occurred in the Lower Reach (Figs. 7F and 14A).

5.3.2 Early filling stage

During this stage, turbidity currents supplied by the axial sediment source began to fill the canyon. During the deposition of DU2, thick-bedded high-density turbidity current deposits occurred in the Middle and Lower Reaches, whereas only thin-bedded low-density turbidity current deposits were deposited in the Upper Reach (Fig. 7). Moreover, the thickness of DU2 in the Upper Reach is obviously thinner than that in the Middle and Lower Reaches (Fig. 9B). It could be inferred that large volumes of coarse-grained sediments were transported into the Middle and Lower reaches, and only small volumes of fine-grained sediments were deposited in the Upper Reach (Fig. 14B). This distribution pattern is believed to be controlled by the morphology of the stepped-thalweg slope along the canyon pathway. In the Upper Reach, turbidity currents have larger gravitational potential energy. Under the promotion of the subsequent turbidity currents, they were likely prone to flow downslope and to transport their main sediment loadings into the Lower Reach to gain the steady state.

During the deposition of DU3, low-density turbidity current deposits supplied by the axial sediment source covered the entire canyon. This trend of grain size decrease was likely caused by a decrease in the sediment supply. The thickness of the turbidites in the Upper Reach was still less than that in the other two segments (Fig. 9C), implying that the Upper Reach is still a bypass-dominated zone (Fig.14B). In general, the distribution pattern of sediments within the canyon during this stage was controlled by the morphology of the stepped-thalweg slope along the canyon pathway.

5.3.3 Late filling stage

At the beginning of this stage, the Red River Fault in the western boundary of the Qiongdongnan Basin, which is adjacent to our study area (Fig. 1), shifted from sinistral strike-slip to dextral movement, resulting in high-frequent seismicity in the Qiongdongnan Basin and its surrounding area (Gong et al., 2011). Triggered by the seismicity, destabilization of the slope deposits occurred in our study area (Fig. 12B). The resultant MTD (DU4) flowed downslope and was deposited in the distal part of the Middle Reach and the Lower Reach (Figs. 10 and 14C). Therefore, the canyon was plugged, and negative relief was created updip of the MTD (Fig. 14C), similar to a dammed lake on land. Therefore, the high-density turbidity current deposits (DU4) supplied by the axial sediment source could not be transported downslope until the negative topography was healed (Fig. 14C). It should be noted that because the turbidity currents could not flow into the Lower Reach, sediment bypass in the Upper Reach probably started to disappear, further evidenced by the slightly thickness increasing trend occurring in the Upper Reach and the southwestern part of the Middle Reach (Fig. 9D).

After the MTD topography was healed, high-density turbidity current deposits (DU5) supplied by the axial sediment source were transported downslope again (Figs. 11A and 14D). The thickness of DU5 shows little variation throughout the study area (Fig. 9E). Therefore, the Upper Reach was not a bypass-dominated zone, although the turbidity currents could flow downslope again. It should be noted that the high-density turbidity current deposits could not cover the Lower Reach and the distal part of the Middle Reach owing to surface ponding atop the MTD (Fig. 11). Coarse-grained sediments were distributed mainly in the lower parts of the turbidity currents and were confined within the negative topography atop the MTD. Only the upper dilute turbidity currents could have reached the topographic highs, such as that occurring through the interaction between turbidity currents and debris topography as documented by Armitage et al. (2009) in the

Upper Cretaceous Tres Pasos Formation exposed on the Sierra Contreras (southern Chile), By Gamboa et al. (2010) in the Espírito Santo Basin during the Palaeogene, SE Brazil, and by Masalimova et al. (2015) in the Puchkirchen Formation in the Molasse Basin (Austria). The deposition of DU5 led to the complete infilling of the Upper Reach.

Afterwards, slope oversteepening resulting from rapid slope progradation (Fig. 12B) and the seismicity resulting from the Red River Fault activity (Gong et al., 2011) triggered the large volumes of MTCs that flowed downslope and were deposited in the Middle and Lower reaches (DU6) (Figs. 12A and 14E). The same phenomenon was also observed in the adjacent Lingshui Depression of the Qiongdongnan Basin (Gong et al., 2011, 2014; Wu et al., 2018). This resulted in a sharp decrease in canyon accommodation space and the abrupt step of the deepest part of the remanent canyon to the southeast with a maximum distance of 10.69 km (Figs. 12A). After the deposition of DU6, the shallow and wide canyon was filled completely by turbidites supplied by the axial sediment source (Figs. 12 and 14F). During this stage, the canyon fillings generally show a complex interplay among the axial and sediment source and the topographic changes.

Comparing to the early filling stage, a smaller sediment input from the axial sediment source during the late filling stage is present. This phenomenon is in agreement with relative sea-level changes in the Qiongdongnan Basin. Between 8.2 Ma (T31) and 5.7 Ma (T30) when the Central Canyon was experiencing the early filling stage, the relative sea level was low (Fig. 2). Therefore, abundant sediments supplied by the axial sediment source could be transported from the continental shelf into the Central Canyon. However, the period between 5.7 Ma (T30) and 4.2 Ma (T29 Ma) during which the canyon was going through the late filling stage, the relative sea level rose (Fig. 2). Thus, sediment input from the axial sediment source decreased. This phenomenon has been well documented in the previous studies, such as the Kushiro submarine canyon documented by Tuzino et al. (2010) in the Kurile Trench forearc slope (northwestern Pacific), and the canyon documented by Di Celma et al. (2011) in the Peri-Adriatic basin (central Italy). The increased sediment input from the northern continental slope should be attributed to rapid slope progadation that resulted in slope oversteepening, and the seismicity resulting from the Red River Fault activity (e.g. Gong et al. 2011). These factors gave rise to the frequent slope failures so that large volumes of MTDs flowed into the canyon during the late filling stage. All in all, variations in the amount and direction of sediment supplies, and the stepped paleotopography controlled the depositional architecture of the Central Canyon.

6. Conclusions

(1) The Central Canyon developed along the thalweg of a stepped palaeotopography during the Late Miocene and its relief resulted from the tectonic framework and associated sedimentation. A stepped slope and variation in the thalweg-extending direction lead to the changes in the incising depth and width of the canyon.

(2) The canyon fillings consist of relatively coarse-grained turbidites supplied by the axial sediment source and fine-grained MTDs supplied by the canyon-side sediment source. The turbidites are characterized by thick-bedded medium-grained or fine-grained sandstones or siltstones interbedded with mudstone, whereas the MTDs are dominated by mudstones originated from the northern slope of the Qiongdongnan basin.

(3) Three evolutional phases of canyon development are distinguished, namely the incising stage (Stage 1), the early filling stage (Stage 2) and the late filling stage (Stage 3). During the incising stage, the formation of incising canyon was attributed to a stepped paleotopography and sea-level fall during the Late Miocene. High-energy erosive turbidity currents scoured and incised significantly along the thalweg, and initiated the formation of the Central Canyon. Subsequently or contemporaneously, the sharp bend at the beginning of the Middle Reach likely resulted in lateral erosion, which triggered large-scale and small-scale canyon margin failures in both the Middle and Lower Reaches, respectively. During the subsequent early filling stage (Stage 2), the canyon infillings were dominated by the turbidite deposition supplied by the axial sediment source from the Central Vietnam and the western Hainan Island. Controlled by the morphology of the stepped-thalweg slope along the canyon pathway, the Upper Reach of the canyon is a bypass-dominated zone. However, the canyon fillings were dominated by MTDs interbedded with thin-layer turbidite deposits in the late filling stage (Stage 3). Finally, the increase of MTDs from the northern continental slope and the decrease of turbidite deposits from the axial sediment source upwards led to the completely infilling of the canyon. Such variations in architecture of the canyon along its pathway were believed to be controlled by multiple sediment supplies and topographic changes.

Acknowledgments

We would like to thank China National Offshore Oil Company (CNOOC) for providing high resolution 2D and 3D seismic data together with well logs and lithological data. The authors also express their appreciations for the help provided by colleagues of the CNOOC, and College of Marine Science and Technology, China University of Geosciences (Wuhan). Two reviewers are also thanked for their constructive comments and suggestions. This study is supported by the National Natural Science Foundation of China (Nos. 41976067, 41502102, 41606074, 91528301, and 41676051), the Programme of Introducing Talents of

Discipline to Universities (No. B14031), and the Fundamental Research Funds for the Central Universities, China University of Geosciences (Wuhan) (Nos. CUG170659)

References

Antobreh, A.A., Krastel, S., 2006. Morphology, seismic characteristics and development of Cap Timiris Canyon, offshore Mauritania: a newly discovered canyon preserved-off a major arid climatic region. Mar. Petrol. Geol. 23, 37-59.

Armitage, D.A., Romans, B.W., Covault, J.A., Graham, S.A., 2009. The influence of mass-transport-deposit surface topography on the evolution of turbidite architecture: The Sierra Contreras, Tres Pasos Formation (Cretaceous), Southern Chile. J. Sediment. Res. 79, 287-301.

Baas, J.H., Kesteren, W.V., Postma, G., 2004. Deposits of depletive high-density turbidity currents: a flume analogue of bed geometry, structure and texture. Sedimentology. 51, 1053-1088.

Babonneau, N., Savoye, B., Cremer, M., Klein, B., 2002. Morphology and architecture of the present canyon and channel system of the Zaire deep-sea fan. Mar. Petrol. Geol. 19, 445-467.

Bertoni, C., Cartwright, J., 2005. 3D seismic analysis of slope-confined canyons from Plio-Pleistocene of the Ebro Continental Margin (Western Mediterranean). Basin Res. 17, 43–62.

Bouroullec, R., Weimer, P., 2017. Geometry and kinematics of Neogene allochthonous salt systems in the Mississippi Canyon, Atwater Valley, western Lloyd Ridge, and western DeSoto Canyon protraction areas, northern deep-water Gulf of Mexico. AAPG BULL, 101(7), 1003-1034.

Brooks, H.L., Hodgson, D.M., Brunt, R.L., Peakall, J., Hofstra, M., Flint, S.S., 2018. Deep-water channel-lobe transition zone dynamics: Processes and depositional architecture, an example from the Karoo Basin, South Africa. Bulletin. 130, 1723-1746.

Bull, S., Cartwright, J., Huuse, M., 2009. A review of kinematic indicators from mass-transport complexes using 3D seismic data. Mar. Petrol. Geol. 26, 1132–1151.

Campion, K.M., Sprague, A.R., Mohrig, D., Lovell, R.W., Drzewiecki, P.A., Sullivan, M.D., Ardill, J.A., Jensen, G.N., Sickafoose, D.K., 2000. Outcrop expression of confined channel complexes. In: Weimer, P., Slatt, R.M., Coleman, J., Rosen, N.C., Nelson, H., Bouma, A.H., Styzen, M.J., Lawrence, D.T. (Eds.), Deep-Water Reservoirs of The World. Gulf Coast Section SEPM 20th Bob F. Perkins Research Conference, pp. 127e150.

Canals, M., Lastras, G., Urgeles, R., Casamor, J.L., Mienert, J., Cattaneo, A., De Batist, M., Haflidason, H., Imbo, Y., Laberg, J.S., Locat, J., Long, D., Longva, O., Masson, D.G., Sultan, N., Trincardi, F., Bryn, P., 2004. Slope failure dynamics and impacts from seafloor and shallow sub-seafloor geophysical data: case studies from the COSTA project. Mar. Geol. 213, 9-72.

Cao, L.C., Jiang, T., Wang, Z.F., Zhang, Y.Z., Sun, H., 2015. Provenance of upper Miocene sediments in the Yinggehai and Qiongdongnan basins, northwestern South China Sea: evidence from ree, heavy minerals and zircon U-Pb ages. Mar. Geol. 361, 136-146.

Catterall, V., Redfern, J., Gawthorpe, R., Hansen, D., Thomas, M., 2010. Architecture style and quantification of a submarine channel-levee system located in a structurally complex area: offshore Nile Delta. J. Sediment. Res. 80, 991-1017.

Chen, H., Xie, X.N., Guo, J.L., Su, M., Z, K.Q., Shang, F., Huang, W., Wang, W., Shang, Z.L., 2015. Provenance of Central Canyon in Qiongdongnan Basin as evidenced by detrital zircon U-Pb study of upper Miocene sandstones. Sci. China Earth Sci. 58, 1337-1349.

Crossey, L.J., Ficher, T.P., Jonathan Patchett, P., Karlstrom, K.E., Hilton, D.R., Newell, D.L., Huntoon, P., Reynolds, A.C., Leeuw, G.A.M., 2006. Dissected hydrologic system at the Grand Canyon: interaction between deeply derived fluids and plateau aquifer waters in modern springs and travertine. Geology. 34, 25-28.

Cui, Y.C., Shao, L., Qiao, P.J., Pei, J.X., Zhang, D.J., Tran, H.Y., 2018. Upper Miocene-Pliocene provenance evolution of the Central Canyon in northwestern South China Sea. Mar. Geophys. Res. 1-13.

Deptuck, M.E., Steffans, G.S., Barton, M., Pirmez, C., 2003. Architecture and evolution of upper fan channel-belts on the Niger Delta slope and in the Arabian Sea. Mar. Petrol. Geol. 20, 649-676.

Deptuck, M.E., Sylvester, Z., Pirmez, C., O'Byrne, C., 2007. Migration-aggradation history and 3-D seismic geomorphology of submarine channels in the Pleistocene Benin-major Canyon, western Niger Delta slope. Mar. Petrol. Geol. 24, 406-433.

Di Celma, C., 2011. Sedimentology, architecture, and depositional evolution of a coarse-grained submarine canyon fill from the Gelasian (early Pleistocene) of the Peri-Adriatic basin, Offida, central Italy. Sedimentary Geology, 238(3-4), 233-253.

Di Celma, C., Teloni, R., Rustichelli, A., 2014. Large-scale stratigraphic architecture and sequence analysis of an early Pleistocene submarine canyon fill, Monte Ascensione succession (Peri-Adriatic basin, eastern central Italy). Int. J. Earth Sci. 103, 843–875.

Flecker, R., Krijgsman, W., Capella, W., de Castro Martíns, C., Dmitrieva, E., Mayser, J.P., Marzocchi, A., Modestou, S., Ochoa, D., Simon, D., Tulbure, M., van den Berg, B., van der Schee, M., de Lange, G., Ellam, R., Govers, R., Gutjahr, M., Hilgen, F., Kouwenhoven, T., Lofi, J., Meijer, P., Sierro, F.J., Bachiri, N., Barhoun, N., Alami, A.C., Chacon, B., Flores, J.A., Gregory, J., Howard, J., Lunt, D., Ochoa, M., Pancost, R., Vincent, S., Yousfi, M.Z., 2015. Evolution of the Late Miocene Mediterraneane Atlantic gateways and their impact on regional and global environmental change. Earth-Science Rev. 150, 365-392.

Frey Martinez, J., Cartwright, J., Hall, B., 2005. 3D seismic interpretation of slump complexes: examples from the continental margin of Israel. Basin Res. 17, 83–108.

Fuh, C.S., Chern, C.C., Liang, S.C., Yang, Y.L., Wu, S.H., Chang, T.Y., Lin, J.Y., 2009. The biogenic gas potential of the submarine canyon systems of PlioePeistocene foreland Basin, southwestern Taiwan. Mar. Petrol. Geol. 26, 1087-1099.

Gamberi, F., Rovere, M., Marani, M.P., 2011. Mass-transport complex evolution in a tectonically active margin (Gioia Basin, Southeastern Tyrrhenian Sea). Mar. Geol. 279, 98-110.

Gamberi, F., Rovere, M., Marani, M.P., Dykstra, M., 2015. Modern submarine canyon feeder-system and deep-sea fan growth in a tectonically active margin (northern Sicily). Geosphere. 11, 307–319.

Gamboa, D., Alves, T., Cartwright, J., Terrinha, P., 2010. MTD distribution on a ‘passive’continental margin: the Espírito Santo Basin (SE Brazil) during the Palaeogene. Mar. and Petrol. Geol. 27(7), 1311-1324.

Gingele, F.X., Deckker, P.D., Hillenbrand, C.D., 2004. Late Quaternary terrigenous sediments from the Murray Canyons area, offshore South Australia and their implications for sea level change, palaeoclimate and palaeodrainage of the Murraye Darling Basin. Mar. Geol. 212, 183-197.

Gamboa, D., Alves, T., 2016. Bi-modal deformation styles in confined mass-transport deposits: examples from a salt mini basin in SE Brazil. Mar. Geol. 379, 176–193.

Gong, C.L., Wang, Y.M., Zhu, W.L., Li, W.G., Xu, Q., Zhang, J.M., 2011. The Central Submarine Canyon in the Qiongdongnan basin, northwestern South China Sea: architecture, sequence stratigraphy, and depositional processes. Mar. Petrol. Geol. 28, 1690-1702.

Gong, C.L., Wang, Y.M., David, M.H., Zhu, W.L., Li, W.G., Xu, Q., Li, D., 2014. Origin and anatomy of two different types of mass-transport complexes: A 3D seismic case study from the northern South China Sea margin. Mar. Petrol. Geol. 54, 198-215.

Gong, Z.S., Li, S.T., 1997. Continental margin basin analysis and hydrocarbon accumulation of the northern South China Sea. Science Press, pp. 193-256 (in Chinese with English abstract).

Harris, P.T., Whiteway, T., 2011. Global distribution of large submarine canyons: Geomorphic differences between active and passive continental margins. Mar. Geol. 285(1-4), 69-86.

Huang,W., Xie, X.N., He, Y.L., Wu, J.F., Zhao, Z.G., Wang, X.J., 2015. Evolution and Reservoir Prediction of Yinggehai Formation in western Central Canyon in Qiongdongnan Basin. Acta Sedimentol. Sin. 4, 816-809 (in Chinese with English abstract).

Hu, B., Wang, L.S., Yan, W.B., Liu, S.W., Cai, D.S., Zhang, G.C., Zhong, K., Pei, J.X., Sun, B., 2013. The tectonic evolution of the Qiongdongnan Basin in the northern margin of the South China Sea. J. Asian Earth Sci. 77, 163-182.

Iacono, C.L., Sulli, A., Agate, M., 2014. Submarine canyons of north-western Sicily (Southern Tyrrhenian Sea): Variability in morphology, sedimentary processes and evolution on a tectonically active margin. DEEP-SEA RES PT II. 104, 93-105.

Janocko, M., Nemec, W., Henriksen, S., Warchol, M., 2013. The diversity of deep-water sinuous channel belts and slope valley-fill complexes. Mar. Pet. Geol. 41, 7-34.

Joubert, J.B., Maïtan, V., 2010. Borehole image logs for turbidite facies identification: core calibration and outcrop analogues. First Break. 28(6), 55-66.

Li, C., Ma, M., Lv, C.F., Zhang, G.C., Chen, G.J., Yan, Y.K., Bi, G.X., 2017a. Sedimentary differences between different segments of the continental slope-parallel Central Canyon in the Qiongdongnan Basin on the northern margin of the South China Sea, 2017. Mar. Petrol. Geol. 88, 127-140.

Li, C., Lv, C.F., Chen, G.J., Zhang, G.C., Ma, M., Shen, H.L., Zhao, Z., Guo, S., 2017b. Source and sink characteristics of the continental slope-parallel Central Canyon in the Qiongdongnan Basin on the northern margin of the South China Sea. J. Asian Earth Sci. 134, 1-12.

Li, C., Lv, C.F., Chen, G.J., Zhang, G.C., Ma, M., Yang, H.Z., Bi, G.X., 2019. Zircon U-Pb ages and REE composition constraints on the provenance of the continental slope-parallel submarine fan, western Qiongdongnan Basin, northern margin of the South China Sea. Mar. Petrol. Geol. 102, 350-362.

Li, D., Wang, Y.M., Wang, Y.F., Xu, Q., Wang, J.P., 2011. Sedimentary and foreground of prospect for levee-overbank in the Central Canyon, Qiongdongnan Basin. Acta Sedimentologica Sinica. 29(4), 689-694 (in Chinese with English abstract).

Li, P., Kneller, B.C., Hansen, L., Kane, I.A., 2016. The classical turbidite outcrop at San Clemente, California revisited: an example of sandy submarine channels with asymmetric facies architecture. Sediment. Geol. 346, 1-16.

Li, S.L., Sha, Z.B., Yu, X.H., Cong, X.R., Jiang, L.Y., Wang, J.Z., Fang, J.G., 2013. Impact of Neogene tectonic subsidence characteristics on the BSR distribution in the Qiongdongnan Basin. Geology in China. 1, 163-175 (in Chinese with English abstract).

Li, X.Q., Luke, F.W., Wu, S.G., Ren, J.Y., Zhang, H.J., Quan, X.Y., Jiang, T., Zhang, C., Su, M., He, Y.L., Wang, D.W., 2013. Morphology, sedimentary features, and evolution of a large paleo submarine canyon in Qiongdongnan Basin, Northern South China Sea. J. Asian Earth Sci. 62, 685-696.

Lo Iacono, C., Sulli, A., Agate, M., 2014. Submarine canyons of north-western Sicily (Southern Tyrrhenian Sea): variability in morphology, sedimentary processes and evolution on a tectonically active margin. Deep-Sea Res. II 104, 93–105.

Lowe, D.R., 1982. Sediment gravity flows; II, depositional models with special reference to the deposits of high-density turbidity currents. J. Petrol. 52, 279–297.

Ma, M., Li, C., Lv, C.F., Chen, G.J., Yang, F., Yan, Y.K., Yin, N., Zhang, G.C., 2017. Geochemistry and provenance of a multiple-stage fan in the upper Miocene to the Pliocene in the Yinggehai and Qiongdongnan basins, offshore South China Sea. Mar. Petrol. Geol. 79, 64-80.

Mao, K.N., Xie, X.N., Xie, Y.H., Ren, J.Y., Chen, H., 2015. Post-rift tectonic reactivation and its effect on deep-water deposits in the Qiongdongnan Basin, northwestern South China Sea. Mar. Gephys. Res. 36, 227-242.

Masalimova, L.U.,Lowe, D.R., Mchargue, T., Derksen, R., 2015. Interplay between an axial channel belt, slope gullies and overbank deposition in the Puchkirchen Formation in the Molasse Basin, Austria. Sedimentology. 62, 1717-1748.

Mauffrey, M.A., Urgeles, R., Berné, S., Canning, J., 2017. Development of submarine canyon after the Mid-Pleistocene transition on the Erbo margin, NW Mediterranean: the role of fluvial connections. Quat. Sci. Rev. 158, 77–93.

Mayall, M., Jones, E., Casey, M., 2006. Turbidite channel reservoirs-Key elements in facies prediction and effective development. Mar. Petrol. Geol. 23, 821–841.

Middleton, G.V., Hampton, M.A., 1976. Subaqueous sediment transport and deposition by sediment gravity flows, in Stanley. Marine Sediment Transport and Environmental Management, p. 197-218.

Morley, C.K., 2016. Major unconformities/termination of extension events and associated surfaces in the South China Seas: review and implications for tectonic development. J. Asian Earth Sci. 120, 62-86.

Nagel, D.K., Mullins, H.T., Greene, H.G., 1986. Ascension Submarine Canyon, California-evolution of a multi-head canyon system along a strike-slip continental margin. Mar. Geol. 73, 285–310.

Nardin, T.R., Hein, F.J., Gorsline, D.S., Edwards, B.D., 1979. A review of mass movement processes, sediment and acoustic characteristics and contrasts in slope and base-of-slope systems versus canyon-fan-basin-floor basins, in Doyle. Geology of Continental Slopes: SEPM, Special Publication 27, p. 61–73.

Olafiranye, K., Jackson, C.A.L., Hodgson, D.M., 2013. The role of tectonics and masstransport complex emplacement on upper slope stratigraphic evolution: a 3D seismic case study from offshore Angola. Mar. Pet. Geol. 44, 196-216.

Olariu, M.I., Aiken, C.L.V., Bhattacharya, J.P., Xu, X., 2011. Interpretation of channelized architecture using three-dimensional photo real models, Pennsylvanian deep-water deposits at Big Rock Quarry, Arkansas. Mar. Petrol. Geol. 28, 1157-1170.

Popescua, I., Lericolais, G., Paninc, N., Normand, A., Dinu, C., Drezen, E.L., 2004. The Danube submarine canyon (Black Sea): morphology and sedimentary processes. Mar. Geol. 206, 249-265.

Pratson, L.F., Ryan, W.B.F., Mountain, G.S., Twitchell, D.C., 1994. Submarine canyon initiation by downslope-eroding sediment flows: evidence in late Cenozoic strata on the New Jersey continental slope. Geol. Soc. Am. Bull. 106, 395–412.

Shang, Z.L., Xie, X.N., Li, X.S., Zhang, D.J., He, Y.L., Yang, Xi., Cui, M.Z., 2015. Difference in full-filled time and its controlling factors in the Central Canyon of the Qiongdongnan Basin. Acta Oceanol. Sin. 34, 81-89.

Shipp, R.C., Lu, H., 2011. Impact of a large mass-transport deposit on a field development in the upper slope of southwestern Sabah, Malaysia, offshore northwest Borneo. In: Shipp, R.C., Weimer, P., Posamentier, H. (Eds.), Mass-transport Deposits in Deepwater Settings, SEPM Special Publication, vol. 96, pp. 199-220.

Su, L., Zheng, J.J., Chen, G.J., Zhang, G.C., Guo, J.M., Xu, Y.C., 2012. The upper limit of maturity of natural gas generation and its implication for the Yacheng formation in the Qiongdongnan Basin, China. J. Asian Earth Sci. 54-55, 203-213.

Su, M., Li, J.L., Jiang, T., Tian, S.S., Zhang, C., Xie, X.N., 2009. Morphological features and formation Mechanism of Central Canyon in the Qiongdongnan Basin. Marine Geology and Quaternary Geology. 29, 85–93(in Chinese with English abstract).

Su, M., Xie, X.N., Xie, Y.H., Wang, Z.F., Zhang, C., Jiang, T., He, Y.L., 2014. The segmentations and the significances of the Central Canyon System in the Qiongdongnan Basin, northern South China Sea. J. Asian Earth Sci. 79, 552-563.

Sun, Q.L., Xie, X.N., Piper, D.J.W., Wu, J., Wu, S.G., 2017. Three dimensional seismic anatomy of multi-stage mass transport deposits in the Pearl River Mouth Basin, northern South China Sea: Their ages and kinematics. Mar. Geol. 393, 93-108.

Sun Q.L., Cartwright, L., Xie, X.N., Lu, X.Y., Yuan, S.Q., Chen, C.X., 2018. Reconstruction of repeated Quaternary slope failures in the northern South China Sea. Mar. Geol. 401, 17-35.

Tuzino, T., Noda, A., 2010. Architecture and evolution of the Kushiro submarine canyon in the Kurile Trench forearc slope, North-western Pacific. Sedimentology, 57(2), 611-641.

Umar, M., Khan, A.S., Kelling, G., Kassi, A.M., 2011. Depositional environments of Campaniane-Maastrichtian successions in the Kirthar Fold Belt, southwest Pakistan: tectonic influences on late cretaceous sedimentation across the Indian passive margin. Sediment. Geol. 237, 30-45.

Vesely, F.F., Trzaskos, B., Kipper, F., Assine, M.L., Souza, P.A., 2015. Sedimentary record of a fluctuating ice margin from the Pennsylvanian of western Gondwana: Paraná Basin, southern Brazil. Sediment. Geol. 326, 45-63.

Wang, Y.M., Xu, Q., Li, D., Han, J.H., Lü, M., Wang, Y.F., Li, W.G., Wang, H.R., 2011. Late Miocene red river submarine fan, northwestern South China Sea. Chin. Sci. Bull. 56, 1488–1494.

Wang, Z.F., Sun, Z.P., Zhu, J.T., Guo, M.G., Jiang, R.F., 2015. Natural gas geological characteristics and great discovery of large gas fields in deep-water area of the western South China Sea. Nat. Gas. Ind. 2, 489-498.

Wonham, J.P., Jayr, S., Mougamba, R., Chuilon, P., 2000. 3D sedimentary evolution of a canyon fill (Lower Miocene-age) from the Mandorove Formation, offshore Gabon. Mar. Petrol. Geol. 17, 175-197.

Yoshikawa, S., Nemoto, K., 2010. Seasonal variations of sediment transport to a canyon and coastal erosion along the Shimizu coast, Suruga Bay. Japan. Mar. Geol. 271, 165-176.

Wu, S.G., Yuan, S.Q., Zhang, G.C., Ma, Y.B., Mi, L.J., Xu, N., 2008. Seismic characteristics of a reef carbonate reservoir and implications for hydrocarbon exploration in deep water of the Qiongdongnan Basin, northern South China Sea. Mar. Petrol. Geol. 26, 817-823.

Wu, S.G., Yang, Z., Wang, D.W., Lü, F.L., Lüdmann, T., Fulthorpe, C., Wang, B., 2014. Architecture, development and geological control of the Xisha carbonate platforms, northwestern South China Sea. Mar. Geol. 350, 71-83.

Wu, W. Li, Q., Yu, J., Lin, C.S., Li, D., Yang, T., 2018. The Central Canyon depositional patterns and filling process in east of Lingshui Depression, Qiongdongnan Basin northern South China Sea. Geol. J. 1, 1-18.

Xie, X.N., Müller, R.D., Ren, J.Y., Jiang, T., Zhang, C., 2008. Stratigraphic architecture and evolution of the continental slope system in offshore Hainan, northern South China Sea. Mar. Geol. 247, 129–144.

Yu, J.F., Pei, J.X., Xu, J., 2009. New insight into oil and gas exploration in Miocene and Late Oligocene strata in Qiongdongnan basin. J. Earth Sci. 20, 811-823.

Zhang, D.J., Wang, Y.H., Wang, Z.F., Zuo, Q.M., He, W.J., Zhao, P.X., 2013. Characteristics of sedimentary microfacies in the Central Canyon within the deep water area, Qiongdongnan Basin. Acta Sedimentologica Sinica. 31(6), 1114-1121 (in Chinese with English abstract).

Zhu, M.Z., Graham, S., McHargue, T., 2009. The Red River fault zone in the Yinggehai Basin, South China Sea. Tectonophysics. 476, 397-417.

Zhu, W.L., Huang, B.J, Mi, L.J., Wilkins, R.W.T., Fu, N., Xiao, X.M., 2009. Geochemistry, origin, and deep-water exploration potential of natural gases in the Pearl River Mouth and Qiongdongnan Basins, South China Sea. AAPG BULL. 93, 741-761.

Table 1 Range and average calculations for the morphological parameters of the Central Canyon and thickness of the depositional units (DU1-7)

Reach		Canyon width (km)	Canyon depth (m)	Thickness (m) of the depositional units						
				DU1	DU2	DU3	DU4	DU5	DU6	DU7
Upper Reach	Range	4.1-9.2	288.0-445.5	-	0-255.4	0-210.4	0-150.0	0-130.2	189.2-613.2	0-98.1
	Av.	6.1	378.6	-	44.6	50.4	60.9	62.4	396.9	29.9
Middle Reach	Range	8.8-16.7	282.5-797.2	0-671.0	0-413.5	0-195.1	0-298.7	0-150.6	0-507.9	0-251.0
	Av.	12.5	649.1	152.3	126.7	85.1	131.7	57.0	303.3	89.0
Lower Reach	Range	9.3-11.0	751.5-1032.2	0-266.5	0-435.1	0-225.2	0-270.6	0-122.6	47.54-402.1	0-215.8
	Av.	10.3	919.6	128.7	196.3	91.0	151.3	63.6	321.9	98.0

“ – ” represents non-deposition.

Figure Captions

Fig.1 (A) Present-day topographic map showing the Cenozoic sedimentary basins and the major structures in the northwestern South China Sea, as well as the location of the Central Canyon in the Qiongdongnan Basin (modified after Gong et al., 2011; Mao et al., 2015). The purple dotted lines representing the position of the shelf break at 5.7 Ma (Gong et al., 2011). (B) The map displaying the tectonic units in the western Qiongdongnan Basin (modified after Su et al., 2014) and the locations of wells used in this study (the red dots) and wells used in Cui et al. (2018) (the green dots). The pink solid lines illustrate the positions of the Figures 3A, 3C, 8A, 9A, 12A, 12B, 12C and 13, respectively.

Fig. 2 Cenozoic geological column of the Qiongdongnan Basin with seismic reflectors, structural evolution stages, depositional environments and relative sea-level changes (modified after Su et al., 2014; Wu et al., 2018)

Fig. 3 (A) Topographic map showing the geomorphology of the canyon, and the locations of the measuring lines for the canyon geomorphology-measurements. Also shown are the areas of the Upper, Middle and Lower Reaches of the canyon. (B) Shaded seismic profile (line location shown in Fig. 3A) displaying methodology for quantification. (C) Vertical seismic profile (line shown in Fig. 3A) exhibiting the key seismic reflections (Seabed, T20, T27, T29, T30, T31 and T40, respectively) and four units that was stripped off during the process of decompaction, as well as the position of the Ledong Fan.

Fig. 4 Seismic well tie and synthetic seismic generation from well A and 3D seismic data: (a) TVD (m)/ TWT (ms); (b) Sonic log (μs/ft); (c) Density log (g/cm3); (d) Reflectivity coefficients; (e) Wavelet extracted from the closest seismic profile (inline); (f) Synthetic traces generated using the extracted wavelet; (g) Extracted seismic section (the closest inline); (h) Well tops. Note that, at the location of WellA, DU1 and DU7 did not develop. Therefore, only the tops and bases of DU2-6 were marked.

Fig. 5 Results of quantification of the canyon geomorphology. The canyon thalweg in the first measuring line (i.e. the measuring line in northwestern-most corner of the study area, see Fig. 3A) is referred to the origin of the x-axis. (A) Vertically exaggerated plot along the mapped length of the canyon, showing changes in the thalweg slope gradient and in the canyon depth. (B) Vertically exaggerated plot along the mapped length of the canyon displaying changes in the canyon width.

Fig. 6 Seismic profiles showing seven seismic facies identified in the Central Canyon based on the internal configuration and external geometry of seismic reflections. See the text in Section 4.1 for the detail descriptions.

Fig. 7 (A) Seismic profiles (line location shown in Fig. 1B) along the canyon thalweg showing seven depositional units (DU1 through DU7, upwards) within the canyon filling. (B) Interpretation for the facies organization and distribution within the canyon filling in the seismic profile above. Seismic traverses (location shown in Fig. 1B) showing seven depositional units (DU1-7) within the canyon filling, as well as their facies organization and distribution (C, D, E and F, respectively). MTD= Mass transport deposits.

Fig. 8 (A) Flattened horizontal coherence slice (see the location in Figs. 8B and C) illustrating plan-view geomorphological expression of three slide blocks within DU1. Seismic traverses (location shown in Fig. 8A) showing seismic appearance of the slide blocks (B and C, respectively).

Fig. 9 Isopach maps of the depositional units (DU1-7). Note that, within DU2 (Fig. 9B) and DU3 (Fig. 9C), the obviously thinner thicknesses are present in the Upper reach. In DU4 (Fig. 9D), a slight thickness increasing trend can be observed in the Upper Reach and the southwestern part of the Middle Reach, while the remaining part is characterized by uniform thickness along the canyon pathway. In DU5 (Fig. 9E), relatively uniform thickness is present and the channel-like anomalies is resulted from the velocity model. Within DU6 (Fig. 9F), a thickness reducing trend from the northwest to southeast is present in the Middle and Lower Reaches. In DU7 (Fig. 9G), a thickness increasing trend is present along the canyon pathway.

Fig. 10 (A) Flattened horizontal coherence slice seen at 50 ms above the basal bounding surface (T30) of DU4 illustrating coherence slice appearance of the high-density turbidity current deposits supplied by the axial sediment source and the MTD supplied by the side sediment source, respectively. (B) RMS map of DU4 showing RMS appearance of the high-density turbidity current deposits supplied by the axial sediment source and the MTD supplied by the side sediment source, respectively. MTD= Mass transport deposits.

Fig. 11 (A) RMS map of DU5 showing the RMS appearance of the high-density turbidity current deposits supplied by the axial sediment source. (B) Vertical seismic profile (line location shown in Fig. 11A) illustrating the ponding of turbidites atop the MTD. MTD= Mass transport deposits.

Fig. 12 (A) Flatted horizontal coherence slice (see location in the Fig. 12B) illustrating coherence slice appearance of four MTDs supplied by the canyon-side sediment source within DU6, and low-density turbidity current deposits supplied by the axial sediment source within DU7. (B) Vertical seismic profile (see location in Figs. 1B and 12A) showing the relative positions of the northern continental slope, the southern uplift and the Central Canyon. Also shown is the position of the coherence slice map in Fig. 12A. (C) Seismic profile (line location shown in Fig. 1B) displaying seven depositional units (DU1-7) within the canyon filling and turbidity channel within DU7 in the upper reach. (D) Seismic profile (see location in Fig. 12B) illustrating seismic appearance of DU6 and DU7. MTC= Mass transport complex.

Fig. 13 NE-SW slope-perpendicular profile showing the relative positions of the continental slope, the Ledong Fan and the Central Canyon

Fig. 14 3D depositional evolution models to summarize the filling process and the depositional architecture of the Central Canyon. It evolved through three phases: (1) The incising stage (A); (2) The early filling stage when sediments were supplied by the axial sediment source (B); (3) The late filling stage during which sediments were both supplied by the axial and side sediment sources (C-F). See the text in Section 5.3 for the detail descriptions.

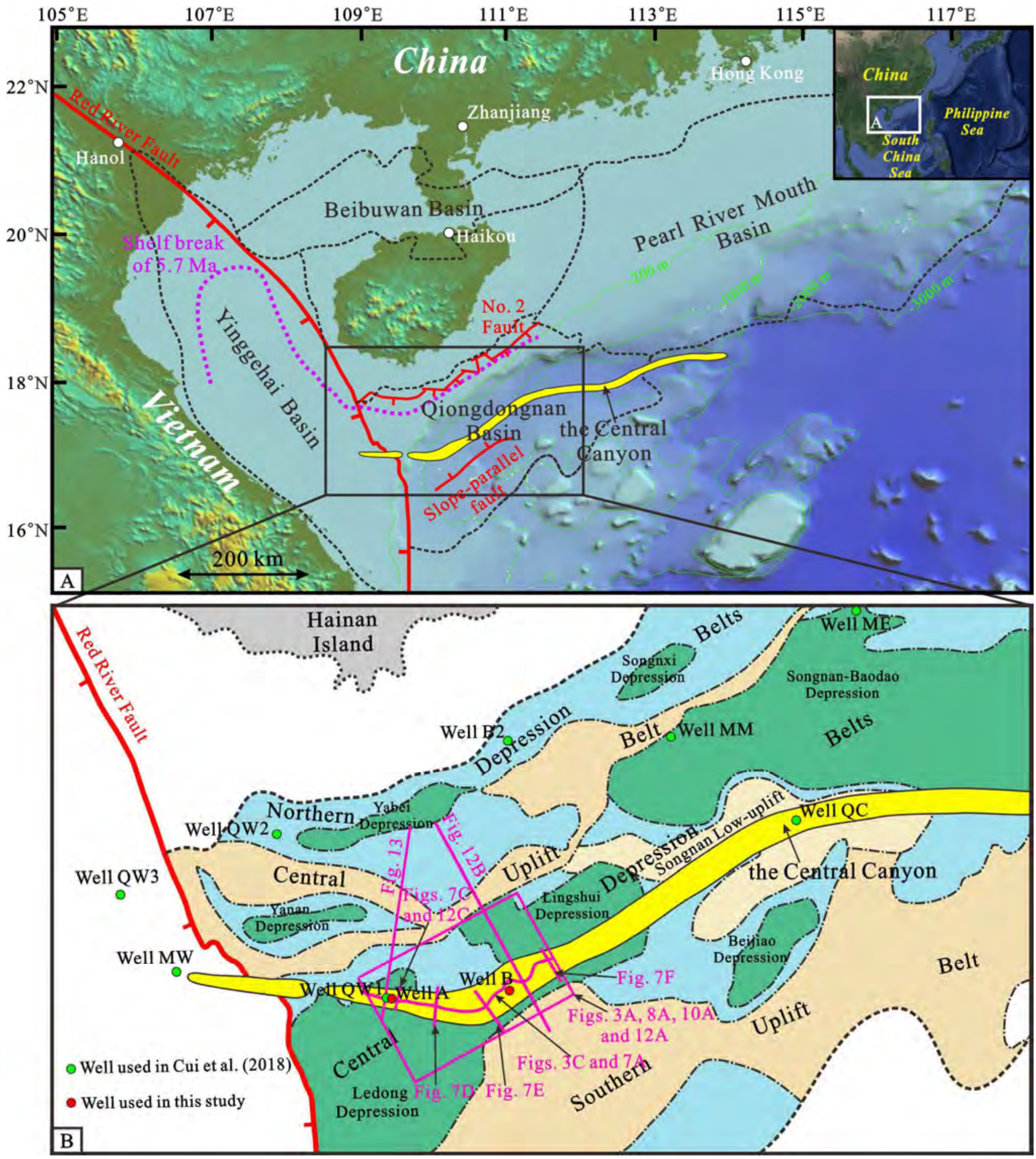

105°E
107°E
109°E
111°E
113°E
115°E
117°E
22°N
20°N
18°N
16°N
China
Hong Kong
Zhanjiang
Hanoi
Red River Fault
Beibuwan Basin
Haikou
Pearl River Mouth Basin
Shelf break of 5.7 Ma
Yinggehai Basin
No. 2 Fault
Qiongdongnan Basin
the Central Canyon
Vietnam
Slope-parallel fault
200 km
A
Philippine Sea
South China Sea
Hainan Island
Belts
Well MF
Songnxi Depression
Songnan-Baodao Depression
Well B2
Depression
Belt
Well MM
Belts
Northern
Yabei Depression
Fig. 12B
Fig. 13
Well QW2
Well QC
Songnan Low-uplift
Well QW3
Central
Uplift
Depression
the Central Canyon
Figs. 7C and 12C
Lingshui Depression
Yanan Depression
Beijiao Depression
Well MW
Well B
Fig. 7F
Belt
Well QW1
Well A
Figs. 3A, 8A, 10A and 12A
Uplift
Central
Figs. 3C and 7A
Well used in Cui et al. (2018)
Well used in this study
Ledong Depression
Fig. 7D
Fig. 7E
Southern
B

Fig. 1

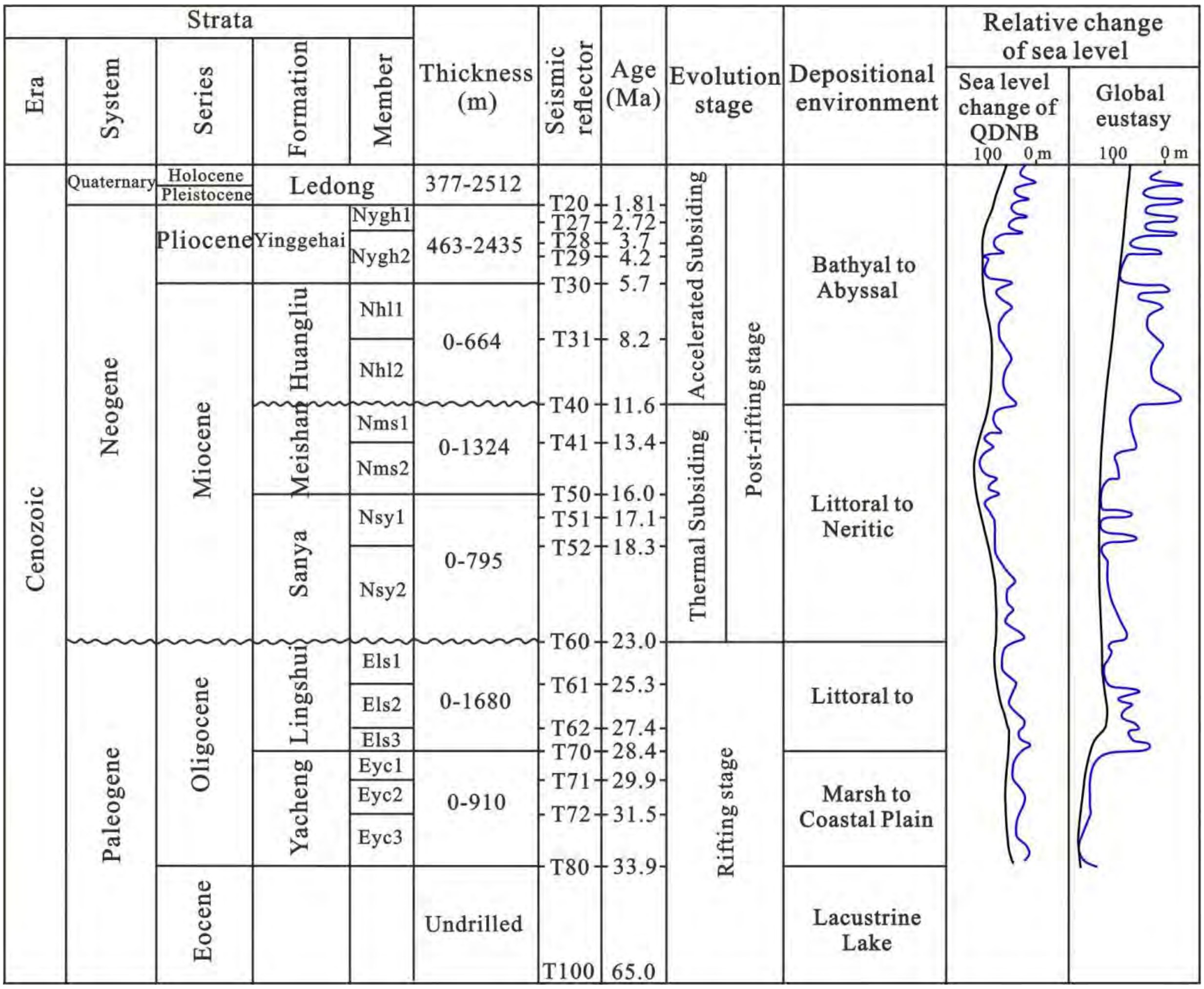
Strata
Era
System
Series
Formation
Member
Thickness (m)
Seismic reflector
Age (Ma)
Evolution stage
Depositional environment
Relative change of sea level
Sea level change of QDNB
Global eustasy
100 0 m
100 0 m
Cenozoic
Quaternary
Holocene
Pleistocene
Ledong
377-2512
Neogene
Pliocene
Yinggehai
Nygh1
Nygh2
463-2435
Miocene
Huangliu
Nhl1
Nhl2
0-664
Meishan
Nms1
Nms2
0-1324
Sanya
Nsy1
Nsy2
0-795
Paleogene
Oligocene
Lingshui
Els1
Els2
Els3
0-1680
Yacheng
Eyc1
Eyc2
Eyc3
0-910
Eocene
Undrilled
T20 1.81
T27 2.72
T28 3.7
T29 4.2
T30 5.7
T31 8.2
T40 11.6
T41 13.4
T50 16.0
T51 17.1
T52 18.3
T60 23.0
T61 25.3
T62 27.4
T70 28.4
T71 29.9
T72 31.5
T80 33.9
T100 65.0
Accelerated Subsiding
Thermal Subsiding
Post-rifting stage
Rifting stage
Bathyal to Abyssal
Littoral to Neritic
Littoral to
Marsh to Coastal Plain
Lacustrine Lake

Fig. 2

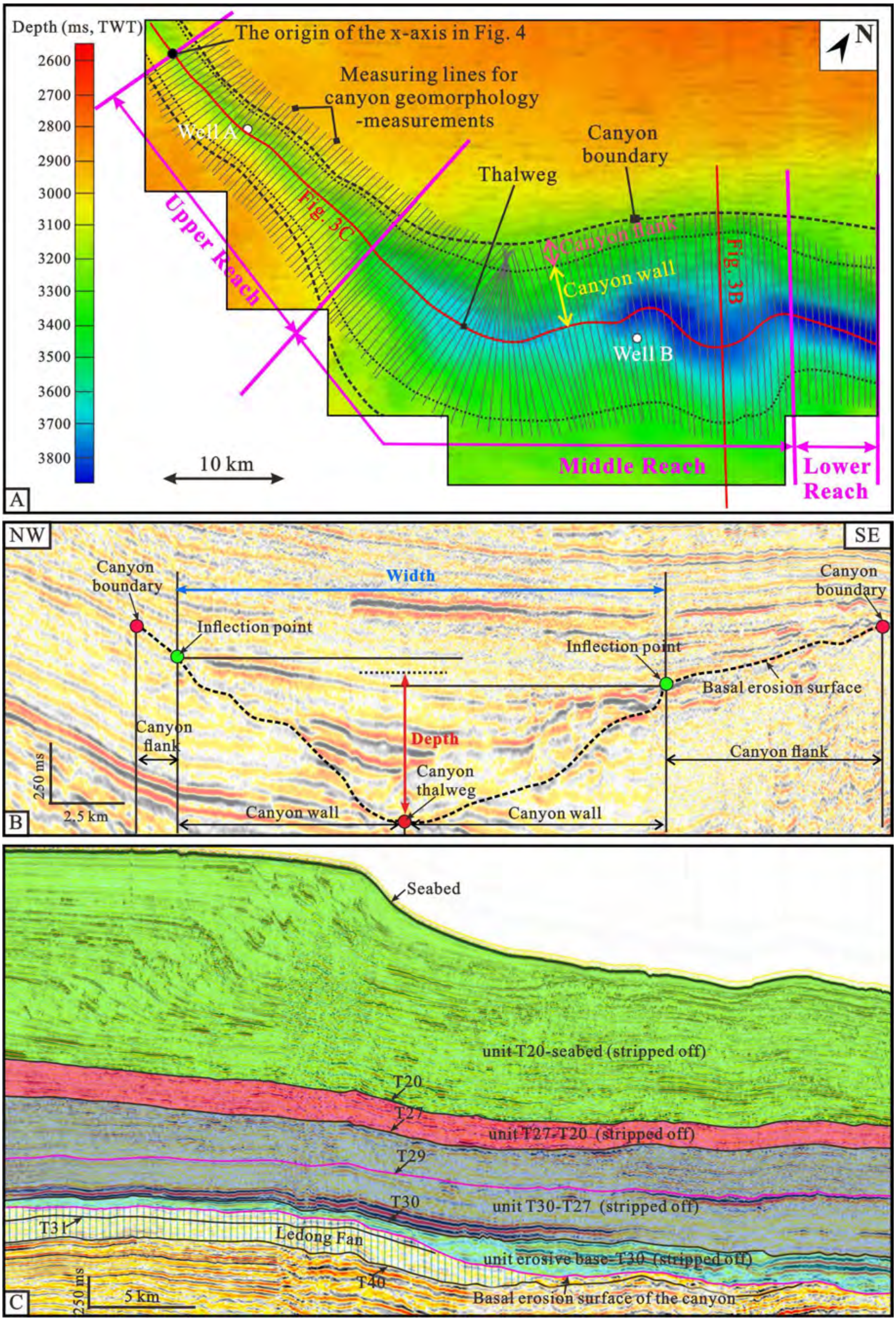
Depth (ms, TWT)
2600
2700
2800
2900
3000
3100
3200
3300
3400
3500
3600
3700
3800
The origin of the x-axis in Fig. 4
Measuring lines for canyon geomorphology -measurements
Well A
Canyon boundary
Thalweg
Fig. 3C
Upper Reach
Canyon flank
Canyon wall
Fig. 3B
Well B
10 km
Middle Reach
Lower Reach
N
A
NW
SE
Canyon boundary
Width
Canyon boundary
Inflection point
Inflection point
Basal erosion surface
Depth
Canyon flank
Canyon flank
Canyon thalweg
250 ms
2.5 km
Canyon wall
Canyon wall
B
Seabed
unit T20-seabed (stripped off)
T20
T27
unit T27-T20 (stripped off)
T29
T30
unit T30-T27 (stripped off)
T31
Ledong Fan
unit erosive base-T30 (stripped off)
T40
250 ms
5 km
Basal erosion surface of the canyon
C

Fig. 3

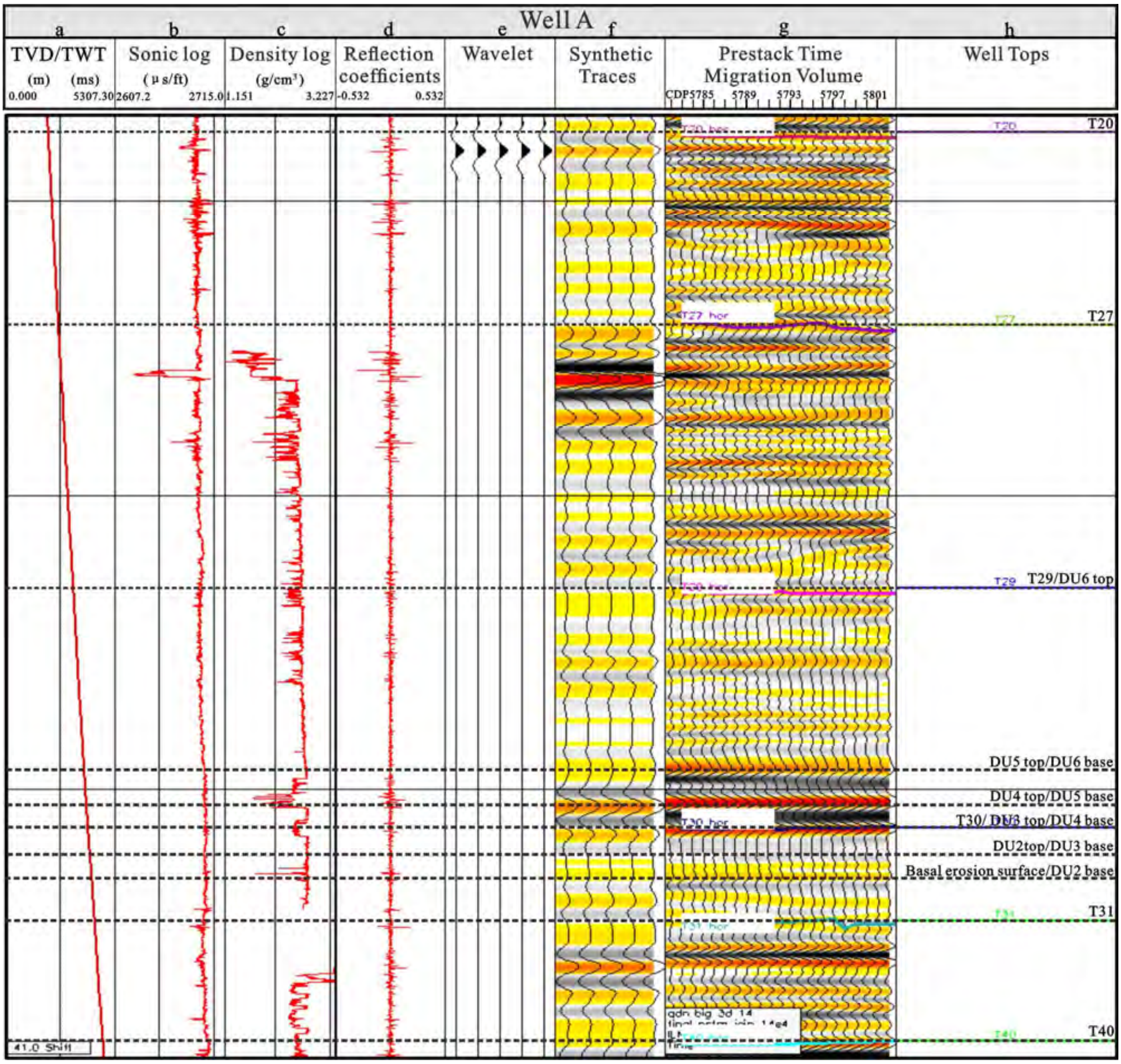
Well A
a
b
c
d
e
f
g
h
TVD/TWT
(m) (ms)
0.000 5307.30
Sonic log
(μs/ft)
2607.2 2715.0
Density log
(g/cm³)
1.151 3.227
Reflection coefficients
-0.532 0.532
Wavelet
Synthetic Traces
Prestack Time Migration Volume
CDP5785 5789 5793 5797 5801
Well Tops
T20
T27
T29/DU6 top
DU5 top/DU6 base
DU4 top/DU5 base
T30/ DU3 top/DU4 base
DU2top/DU3 base
Basal erosion surface/DU2 base
T31
T40
41.0 Shift

Fig. 4

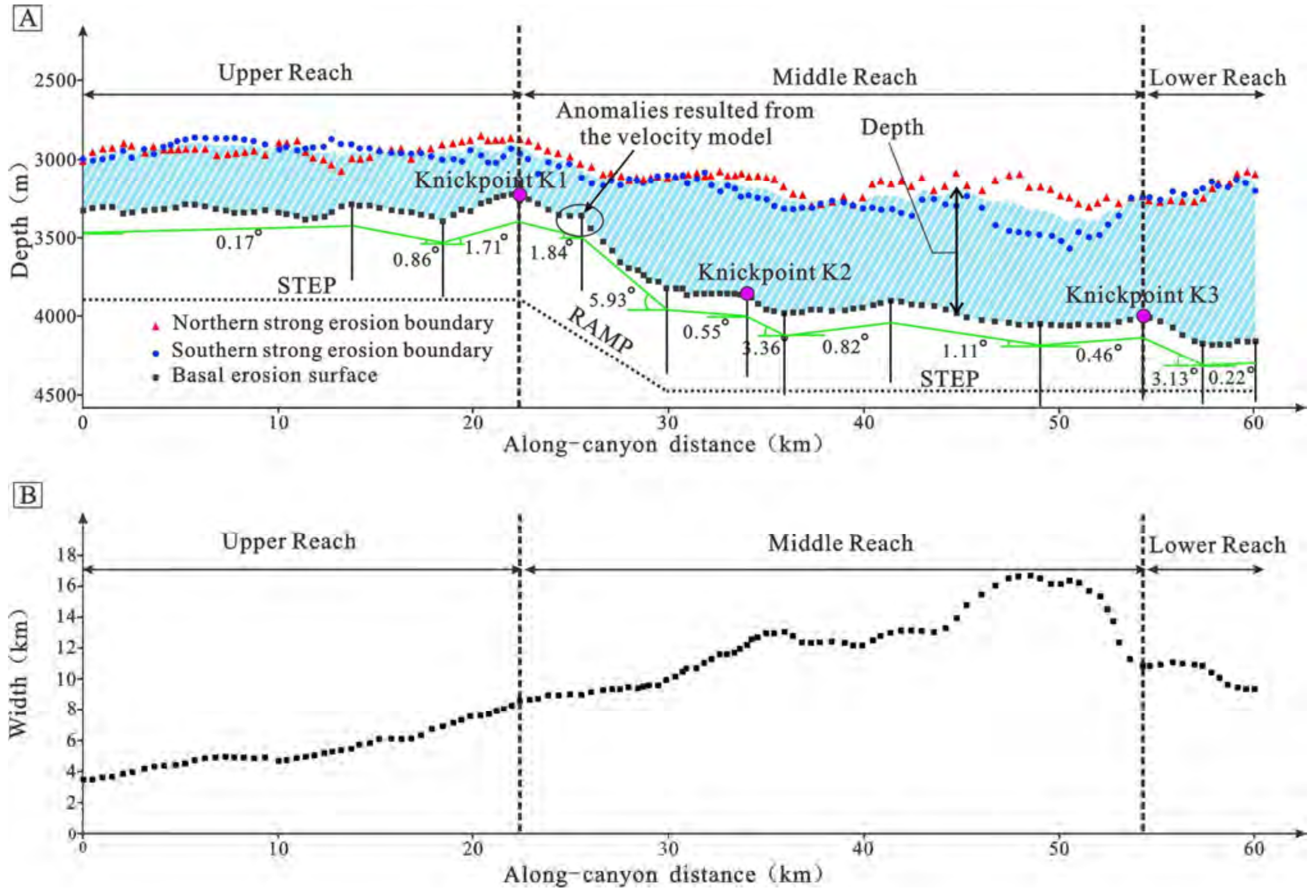
A
Upper Reach
Middle Reach
Lower Reach
Anomalies resulted from the velocity model
Depth
Knickpoint K1
Knickpoint K2
Knickpoint K3
0.17°
0.86°
1.71°
1.84°
5.93°
0.55°
3.36°
0.82°
1.11°
0.46°
3.13°
0.22°
STEP
RAMP
STEP
Northern strong erosion boundary
Southern strong erosion boundary
Basal erosion surface
Depth（m）
Along-canyon distance（km）
B
Upper Reach
Middle Reach
Lower Reach
Width（km）
Along-canyon distance（km）

Fig. 5

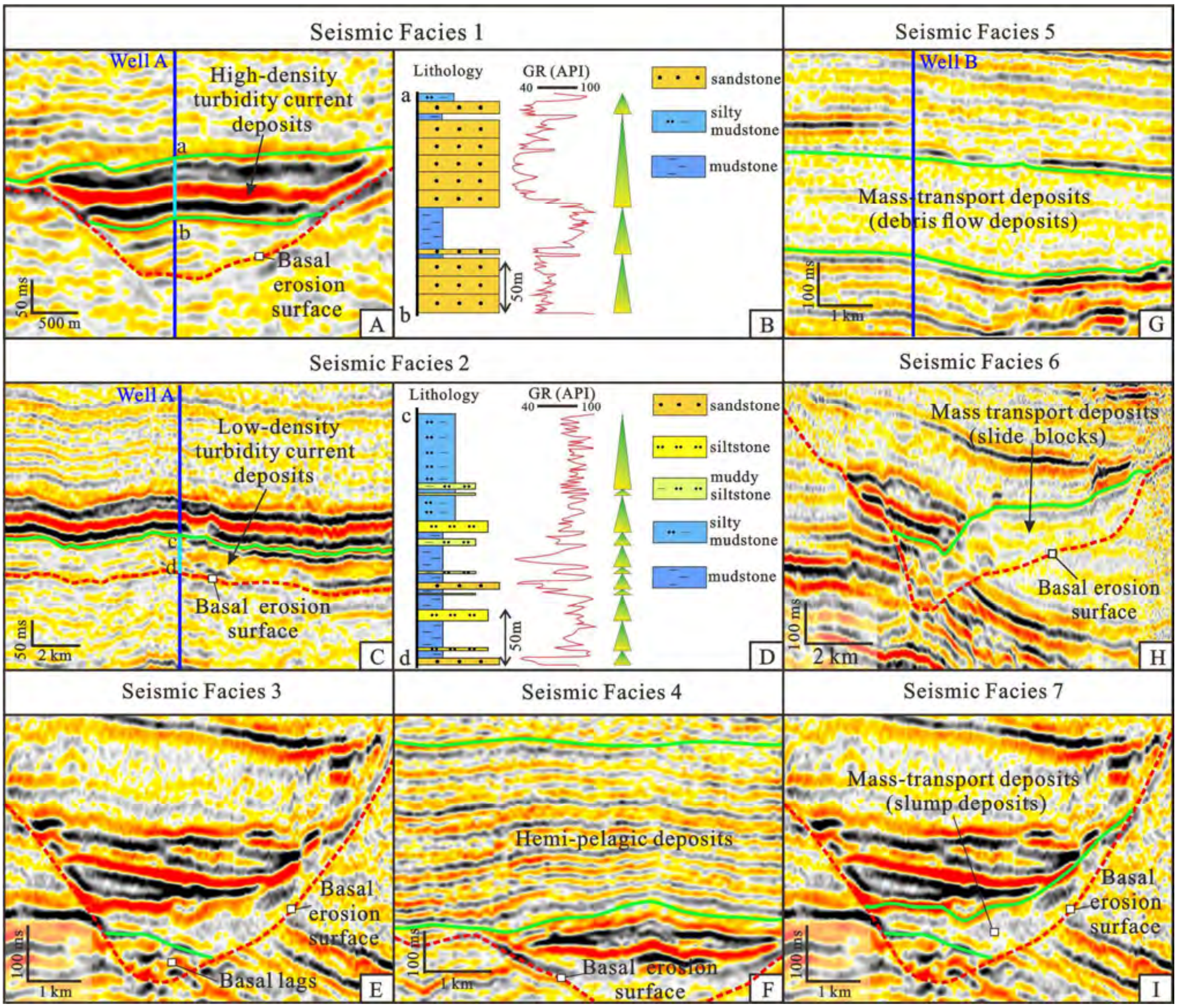

Seismic Facies 1
Well A
High-density turbidity current deposits
a
b
Basal erosion surface
50 ms
500 m
A
Lithology
GR (API)
40
100
50m
sandstone
silty mudstone
mudstone
B
Seismic Facies 5
Well B
Mass-transport deposits (debris flow deposits)
100 ms
1 km
G
Seismic Facies 2
Well A
Low-density turbidity current deposits
c
d
Basal erosion surface
50 ms
2 km
C
Lithology
GR (API)
40
100
50m
sandstone
siltstone
muddy siltstone
silty mudstone
mudstone
D
Seismic Facies 6
Mass transport deposits (slide blocks)
Basal erosion surface
100 ms
2 km
H
Seismic Facies 3
Basal erosion surface
Basal lags
100 ms
1 km
E
Seismic Facies 4
Hemi-pelagic deposits
Basal erosion surface
100 ms
1 km
F
Seismic Facies 7
Mass-transport deposits (slump deposits)
Basal erosion surface
100 ms
1 km
I

Fig. 6

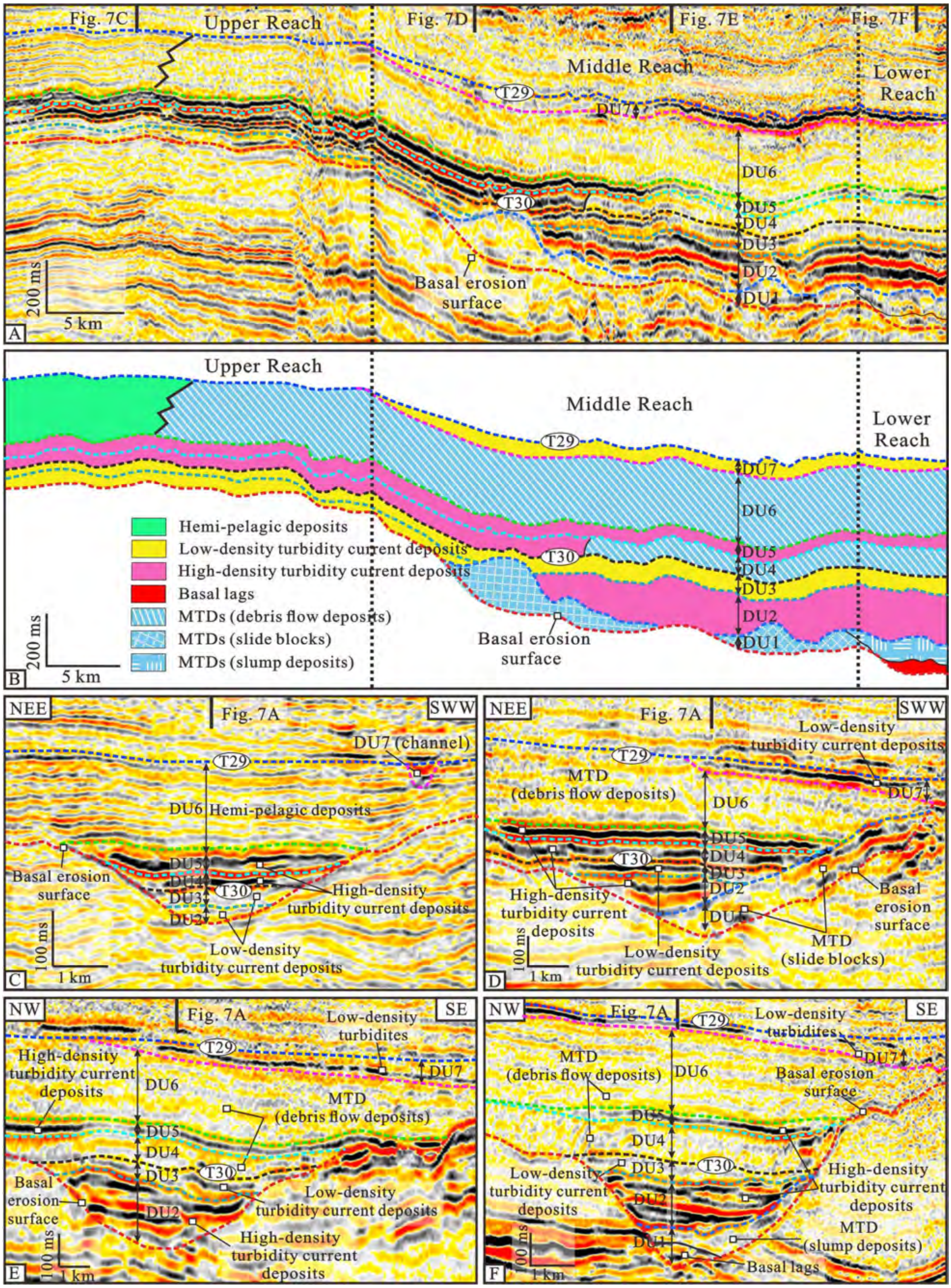
Fig. 7C
Upper Reach
Fig. 7D
Fig. 7E
Fig. 7F
Middle Reach
Lower Reach
T29
DU7
DU6
T30
DU5
DU4
DU3
DU2
DU1
Basal erosion surface
200 ms
5 km
A
Upper Reach
Middle Reach
Lower Reach
T29
DU7
DU6
T30
DU5
DU4
DU3
DU2
DU1
Hemi-pelagic deposits
Low-density turbidity current deposits
High-density turbidity current deposits
Basal lags
MTDs (debris flow deposits)
MTDs (slide blocks)
MTDs (slump deposits)
Basal erosion surface
200 ms
5 km
B
NEE
Fig. 7A
SWW
DU7 (channel)
T29
DU6 Hemi-pelagic deposits
Basal erosion surface
DU5
DU4
T30
DU3
DU2
High-density turbidity current deposits
Low-density turbidity current deposits
100 ms
1 km
C
NEE
Fig. 7A
SWW
Low-density turbidity current deposits
T29
MTD (debris flow deposits)
DU6
DU7
DU5
DU4
T30
DU3
DU2
DU1
High-density turbidity current deposits
Low-density turbidity current deposits
MTD (slide blocks)
Basal erosion surface
100 ms
1 km
D
NW
Fig. 7A
SE
Low-density turbidites
High-density turbidity current deposits
T29
DU7
DU6
MTD (debris flow deposits)
DU5
DU4
DU3
T30
Basal erosion surface
DU2
Low-density turbidity current deposits
High-density turbidity current deposits
100 ms
1 km
E
NW
Fig. 7A
T29
Low-density turbidites
SE
MTD (debris flow deposits)
DU6
DU7
Basal erosion surface
DU5
DU4
DU3
T30
Low-density turbidity current deposits
DU2
High-density turbidity current deposits
MTD (slump deposits)
DU1
Basal lags
100 ms
1 km
F

Fig. 7

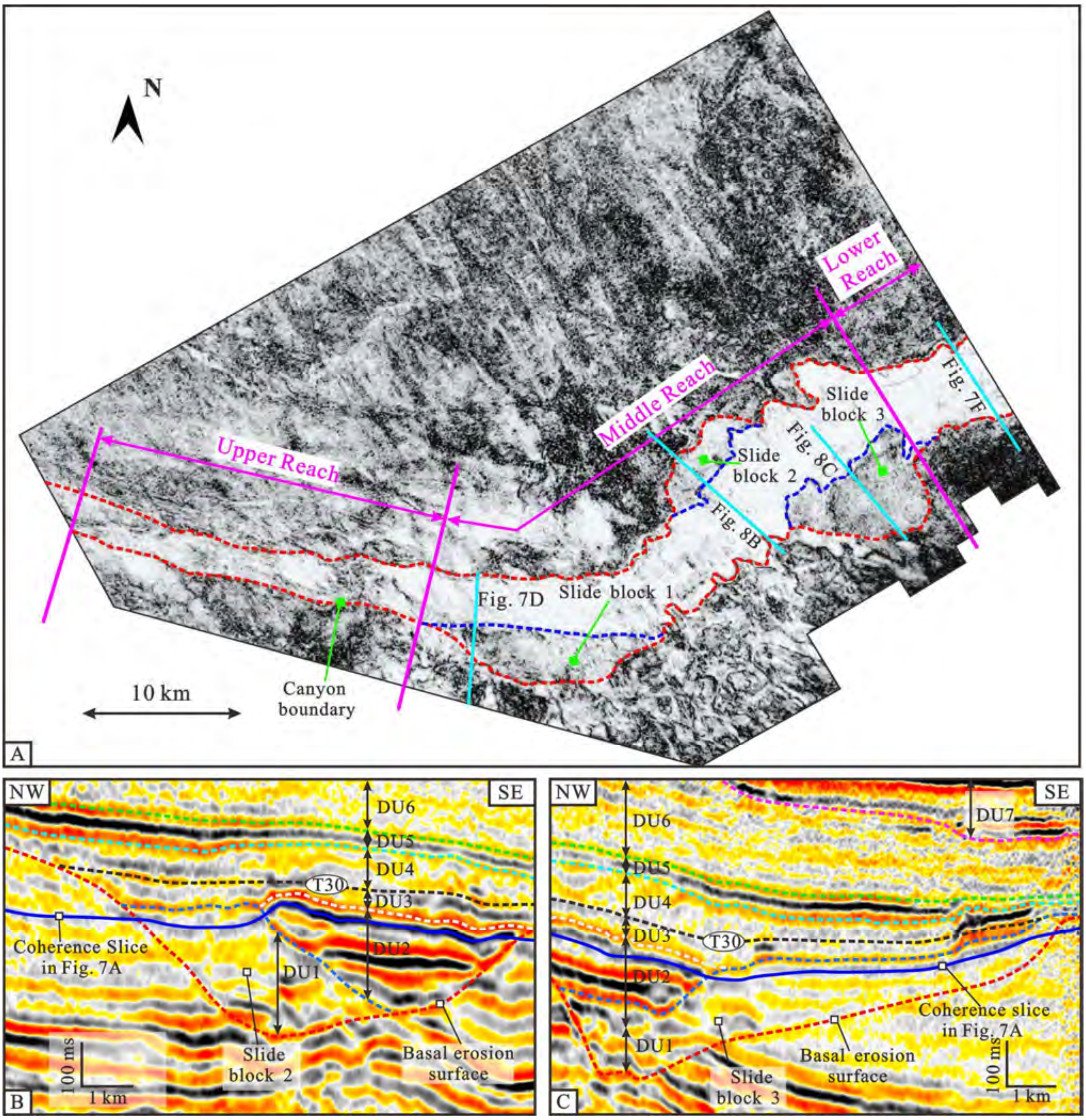
N
Upper Reach
Middle Reach
Lower Reach
Slide block 1
Slide block 2
Slide block 3
Fig. 7D
Fig. 8B
Fig. 8C
Fig. 7F
Canyon boundary
10 km
A
NW
SE
DU6
DU5
DU4
DU3
DU2
DU1
T30
Coherence Slice in Fig. 7A
Slide block 2
Basal erosion surface
100 ms
1 km
B
DU7
Slide block 3
Coherence slice in Fig. 7A
C

Fig. 8

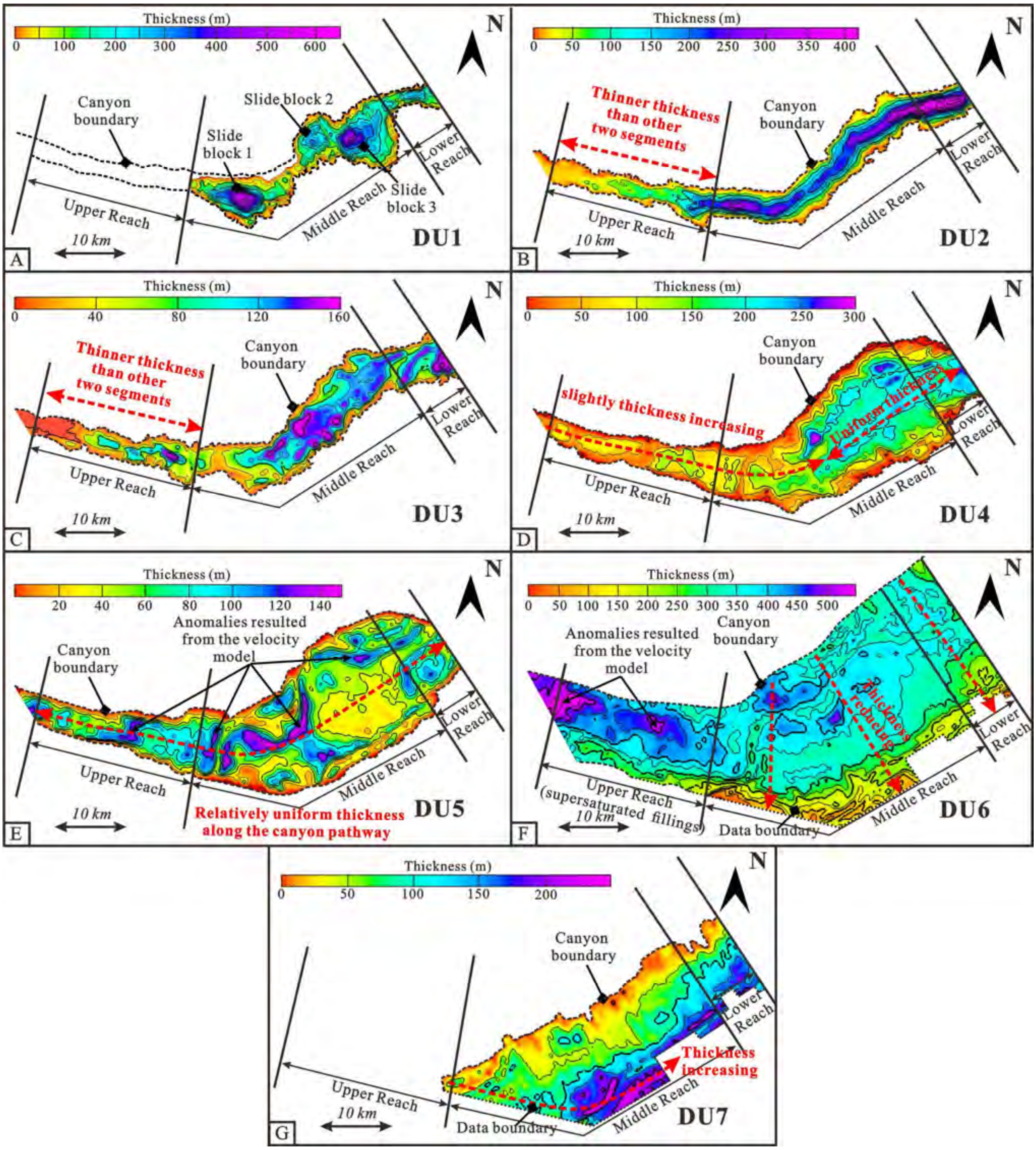

Thickness (m)
N
Canyon boundary
Slide block 1
Slide block 2
Slide block 3
Upper Reach
Middle Reach
Lower Reach
10 km
DU1
Thinner thickness than other two segments
DU2
DU3
slightly thickness increasing
Uniform thickness
DU4
Anomalies resulted from the velocity model
Relatively uniform thickness along the canyon pathway
DU5
Upper Reach (supersaturated fillings)
Data boundary
Thickness reducing
DU6
Thickness increasing
DU7

Fig. 9

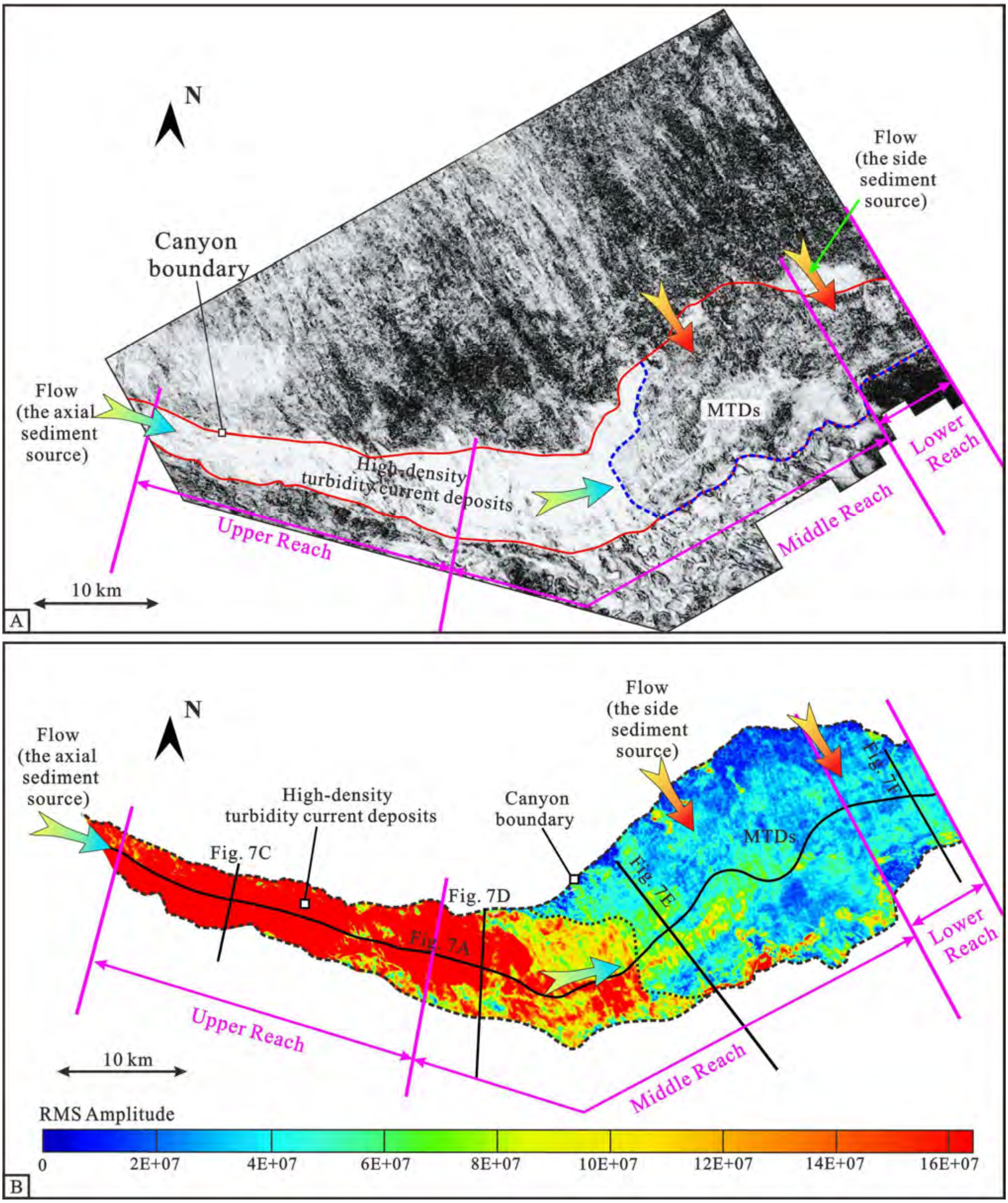
N
Canyon boundary
Flow (the side sediment source)
Flow (the axial sediment source)
MTDs
High-density turbidity current deposits
Upper Reach
Middle Reach
Lower Reach
10 km
A
N
Flow (the axial sediment source)
Flow (the side sediment source)
High-density turbidity current deposits
Canyon boundary
Fig. 7C
Fig. 7D
Fig. 7A
Fig. 7E
Fig. 7F
MTDs
Upper Reach
Middle Reach
Lower Reach
10 km
RMS Amplitude
0
2E+07
4E+07
6E+07
8E+07
10E+07
12E+07
14E+07
16E+07
B

Fig. 10

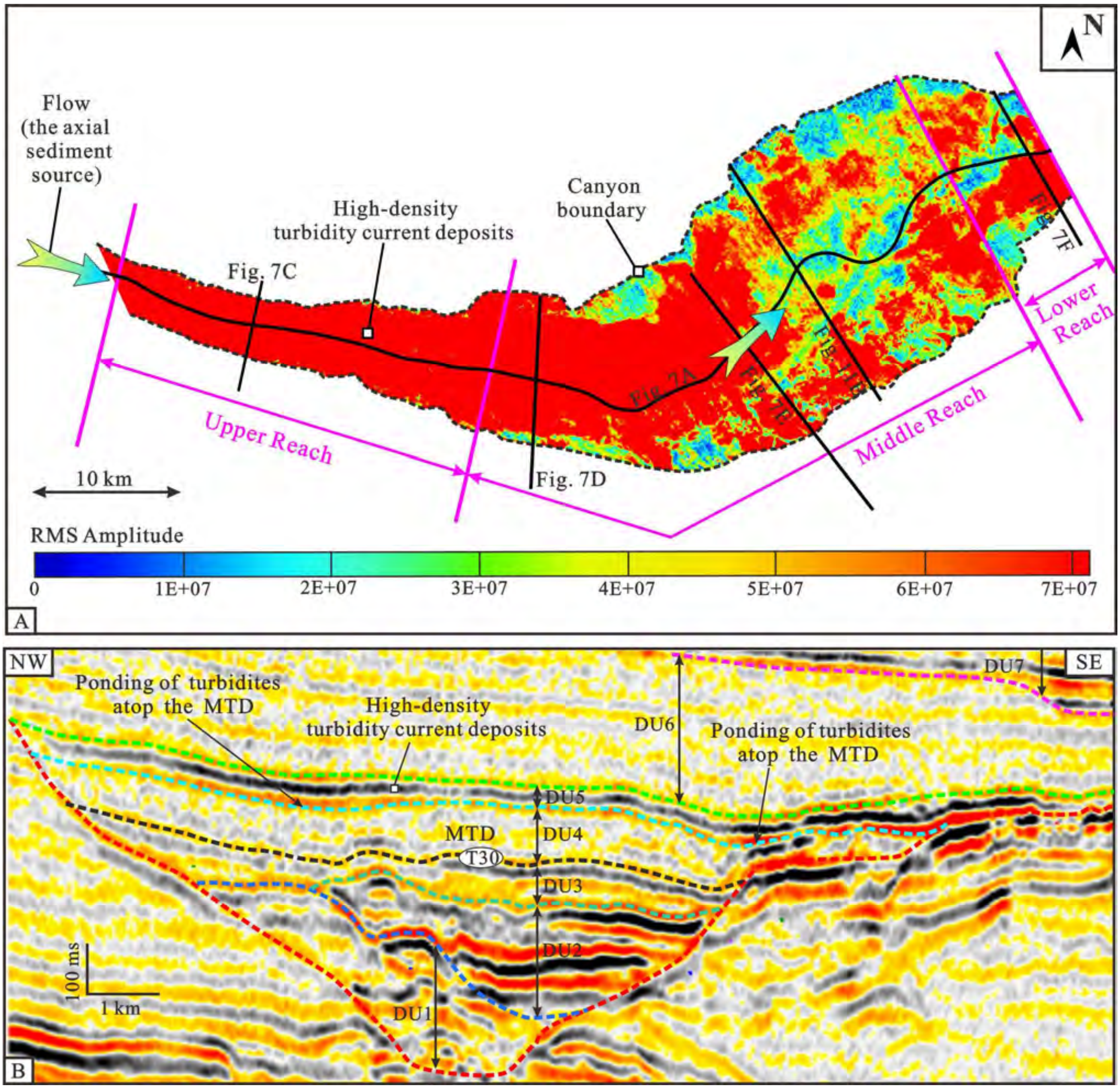

N
Flow
(the axial
sediment
source)
High-density
turbidity current deposits
Canyon
boundary
Fig. 7C
Fig. 7A
Fig. 7D
Fig. 7E
Fig. 7F
Upper Reach
Middle Reach
Lower
Reach
10 km
RMS Amplitude
0
1E+07
2E+07
3E+07
4E+07
5E+07
6E+07
7E+07
A
NW
SE
DU7
Ponding of turbidites
atop the MTD
High-density
turbidity current deposits
DU6
Ponding of turbidites
atop the MTD
DU5
DU4
MTD
T30
DU3
DU2
DU1
100 ms
1 km
B

Fig. 11

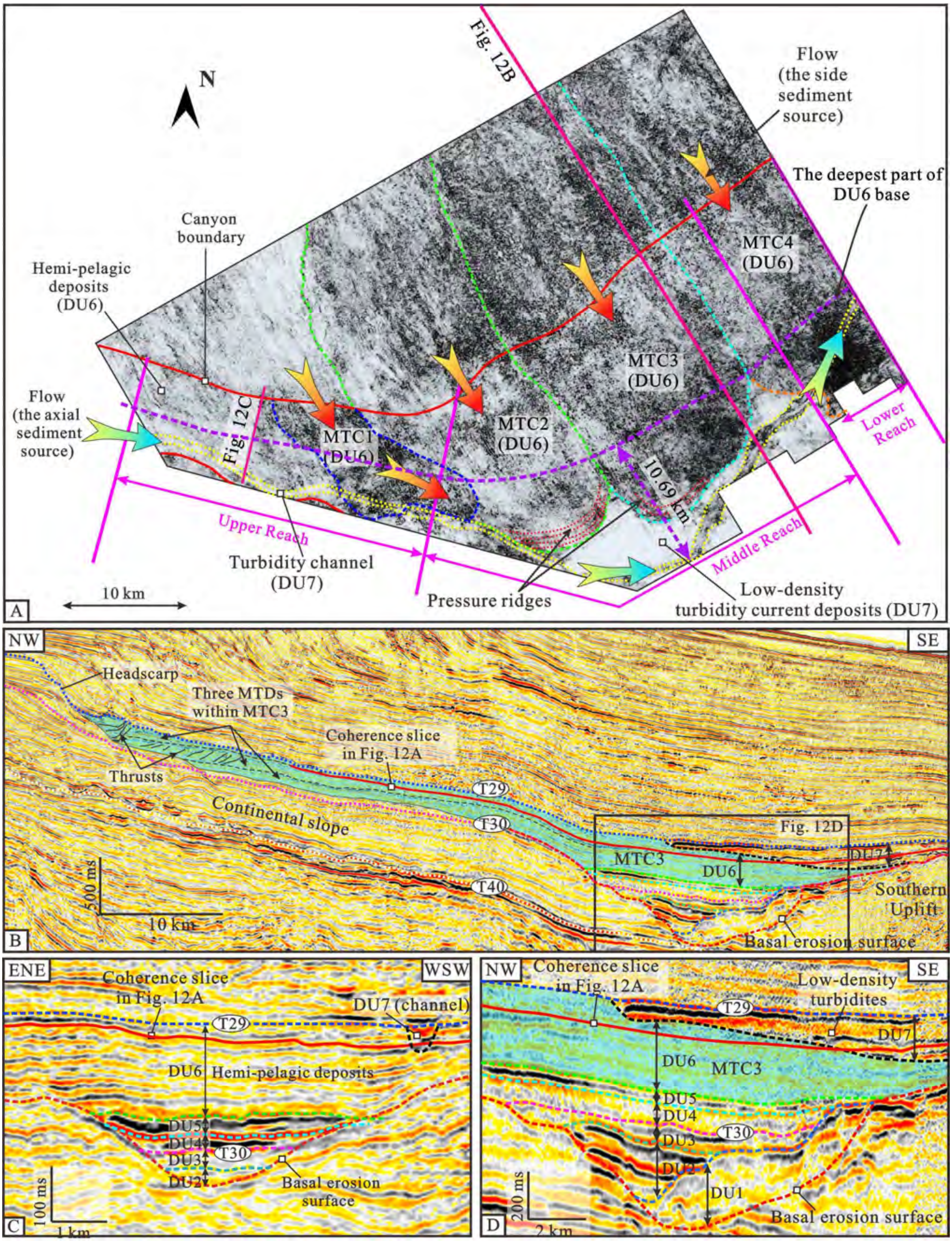
N
Fig. 12B
Flow
(the side
sediment
source)
The deepest part of
DU6 base
Canyon
boundary
Hemi-pelagic
deposits
(DU6)
MTC4
(DU6)
MTC3
(DU6)
MTC2
(DU6)
MTC1
(DU6)
Fig. 12C
Flow
(the axial
sediment
source)
10.69 km
Lower
Reach
Middle Reach
Upper Reach
Turbidity channel
(DU7)
Pressure ridges
Low-density
turbidity current deposits (DU7)
10 km
A
NW
SE
Headscarp
Three MTDs
within MTC3
Thrusts
Coherence slice
in Fig. 12A
T29
Continental slope
T30
Fig. 12D
MTC3
DU6
DU7
T40
500 ms
10 km
Southern
Uplift
Basal erosion surface
B
ENE
WSW
Coherence slice
in Fig. 12A
T29
DU7 (channel)
DU6 Hemi-pelagic deposits
DU5
DU4
DU3
DU2
T30
Basal erosion
surface
100 ms
1 km
C
NW
SE
Coherence slice
in Fig. 12A
T29
Low-density
turbidites
DU7
DU6
MTC3
DU5
DU4
T30
DU3
DU2
DU1
200 ms
2 km
Basal erosion surface
D

Fig. 12

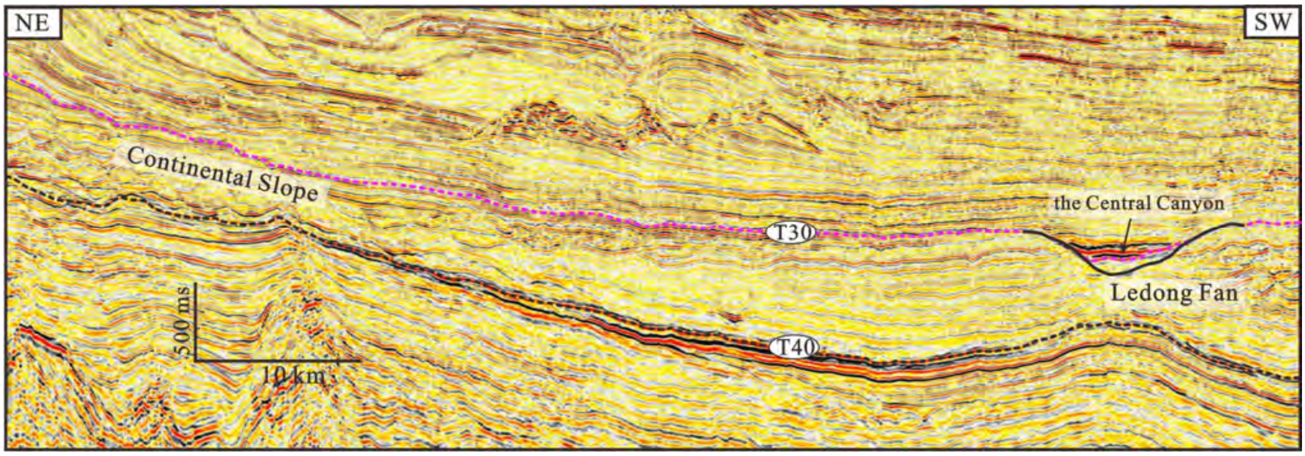
NE
SW
Continental Slope
the Central Canyon
T30
Ledong Fan
500 ms
T40
10 km

Fig. 13

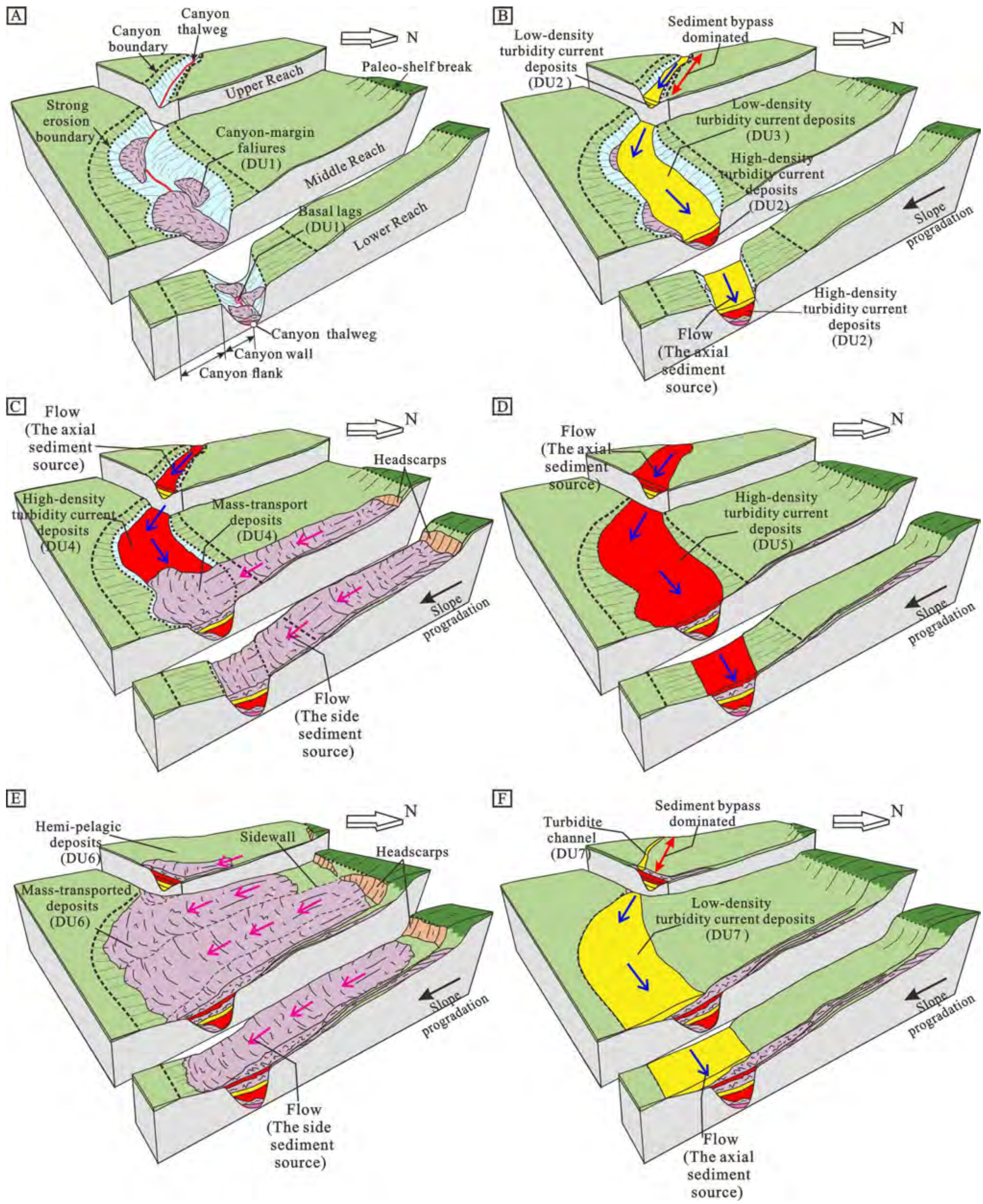
A
Canyon boundary
Canyon thalweg
N
Upper Reach
Paleo-shelf break
Strong erosion boundary
Canyon-margin faliures (DU1)
Middle Reach
Basal lags (DU1)
Lower Reach
Canyon thalweg
Canyon wall
Canyon flank
B
Low-density turbidity current deposits (DU2)
Sediment bypass dominated
N
Low-density turbidity current deposits (DU3)
High-density turbidity current deposits (DU2)
Slope progradation
High-density turbidity current deposits (DU2)
Flow (The axial sediment source)
C
Flow (The axial sediment source)
N
Headscarps
High-density turbidity current deposits (DU4)
Mass-transport deposits (DU4)
Slope progradation
Flow (The side sediment source)
D
Flow (The axial sediment source)
N
High-density turbidity current deposits (DU5)
Slope progradation
E
Hemi-pelagic deposits (DU6)
Sidewall
N
Headscarps
Mass-transported deposits (DU6)
Slope progradation
Flow (The side sediment source)
F
Turbidite channel (DU7)
Sediment bypass dominated
N
Low-density turbidity current deposits (DU7)
Slope progradation
Flow (The axial sediment source)

Fig. 14

Highlights

- **Geomorphology of the palaeoslope-parallel Central Canyon in the Qiongdongnan Basin is quantified.**
- **Effects of multiple sediment supplies and physiographic changes on the depositional architecture of the plaeoslope-parallel Central Canyon are documented in detail.**
- **3D depositional evolution models of the Central Canyon are proposed, providing new insights on the stratigraphic architecture of the deep-water canyon.**

Language Editing Services

Registered Office:
Elsevier Ltd
The Boulevard, Langford Lane,
Kidlington, OX5 1GB, UK
Registration No. 331566771

To whom it may concern

The paper "Multiple sediment supplies and physiographic changes control depositional architecture of a paleoslope-parallel canyon in the Qiongdongnan Basin, South China Sea" by Chao Liang was edited by Elsevier Language Editing Services.

Kind regards,

Elsevier Webshop Support

(This is a computer generated advice and does not require any signature)